KEK-PREPRINT-92-31

Fermilab Library
0 1160 0009188 8

34

KEK Preprint 92-31
May 1992
H

PHYSICS AT TeV e^+e^- LINEAR COLLIDERS EXPERIMENTAL ASPECTS

Keisuke FUJII
National Laboratory for High Energy Physics(KEK)
Tsukuba, 305, Japan

ABSTRACT

Physics at future TeV e^+e^- linear colliders are discussed from the experimental point of view. New features such as the parton reconstruction via jet invariant mass method are stressed by illustrative examples. Also treated are potential problems such as beamstrahlung and beam related backgrounds.

ROUTE TO
NAME
LOCATION
RETURN TO FERMI LIBRARY

Talk presented at 2nd KEK Topical Conference on e^+e^- Collision Physics,
KEK, Tsukuba, Japan, Nov.26-29, 1991

National Laboratory for High Energy Physics, 1992

KEK Reports are available from:

Technical Information & Library
National Laboratory for High Energy Physics
1-1 Oho, Tsukuba-shi
Ibaraki-ken, 305
JAPAN

Phone: 0298-64-1171
Telex: 3652-534 (Domestic)
(0)3652-534 (International)
Fax: 0298-64-4604
Cable: KEKOHO

PHYSICS AT TeV e^+e^- LINEAR COLLIDERS EXPERIMENTAL ASPECTS

Keisuke FUJII
National Laboratory for High Energy Physics(KEK)
Tsukuba, 305, Japan

ABSTRACT

Physics at future TeV e^+e^- linear colliders are discussed from the experimental point of view. New features such as the parton reconstruction via jet invariant mass method are stressed by illustrative examples. Also treated are potential problems such as beamstrahlung and beam related backgrounds.

1. Introduction

Our present understanding of nature is best expressed by the standard model which consists of three sectors: the gauge sector(L_{gauge}), the Higgs sector(L_{Higgs}), and the Yukawa sector(L_{Yukawa}). Although this model has been extremely successful, only a little is known of the Higgs and the Yukawa sectors, reflecting the fact that there are two missing particles, Higgs and top, yet to be discovered. These two unknown sectors are responsible for the mass generations of gauge bosons and ferminons without spoiling the renormalizability of the theory. The key role is played here by the spontaneous symmetry breaking which has an energy scale set by the Higgs vacuum expectation value: $v = (\sqrt{2}G_F)^{-1/2} \simeq 1/4$ TeV. The primary motivation of building a TeV linear collider comes from this energy scale. Such a machine should be able to explore the two unknown sectors and to uncover the origin of masses. Of course, experimentalists should be prepared for the totally unexpected. As a matter of fact, even in the relatively well tested gauge sector, the investigation of the gauge boson self-coupling is still not sufficient. If the weak bosons are composite objects, their self-coupling must have some non-gauge pieces. The effect of such anomalous couplings will be enhanced when we go up in the energy. We believe that precision tests of these untested parts lead us to new physics beyond the standard model and such precision tests can be thoroughly carried out only at TeV e^+e^- linear colliders. It should be emphasized that linear collider projects allow us consistent long-term experimental programs starting at energies around $\sqrt{s} \lesssim 400$ GeV and extending up beyond 1 TeV. The importance of initial experiments in the sub-TeV region alone cannot be underestimated, since they will enable us to closely examine top and weak boson self-couplings, and, more importantly, to confrim or rule out one of the most attractive scenarios which is SUSY.

There are a lot of standard model processes to be investigated, as shown in Fig.1, and it is impossible to cover all of them here. Therefore, we will restrict ourselves to only illustrative examples that demonstrate characteristic features of TeV linear collider experiments[1]. Then what are the characteristic features? In the next section, we first answer this question and then select a few representative standard model processes to be discussed in the

subsequent sections. The beam-related backgrounds, a potential problem of linear collider experiments, are treated following the physics simulation studies of the selected channels. The final section summarizes the results and concludes this talk.

2. Characteristic Features of TeV Linear Collider Experiments

The cross sections for charged particle pair productions are of order $1R$ and are proportional to $1/s$, which implies that the signal to noise ratios for the searches of new particles such as heavy quarks, heavy leptons, charginos, sleptons, and squarks are about one before any cuts. The new particle searches in 2-body final states should, therefore, be no problem. This is a good tradition to be inherited from the past and present e^+e^- colliders. For this feature, therefore, there is, perhaps, only one point I should make, the sensitivity of future linear colliders to supersymmetric particles. Fig.2-a) shows the contours for the lighter chargino mass in the plane of the $SU(2)$ gaugino mass M_2, and the Higgsino mixing mass μ, calculated in the framework of the minimal supersymmetric standard model(MSSM). The right axis indicates the gluino mass which is related to M_2 via the GUT condition. We can see that the detection of a 0.5 TeV chargino at linear colliders is roughly equivalent to that of a 2 TeV gluino at hadron colliders such as LHC and SSC. A 1.5 TeV linear collider surpasses the hadron colliders in the discovery potential for gauginos. Fig.2-b) is a similar plot for scalar fermions, this time as a function of M_2 and the common scalar mass m_0. As for the scalar fermions, the hadron colliders and future TeV linear colliders will be complementary.

As mentioned before, the gauge boson self-couplings are not well tested yet. Inclusion of anomalous couplings to these self-couplings spoils the gauge cancellation and gives rise to some deviations from the standard model predictions. Since the gauge cancellation becomes severer and severer with energy, the sensitivity to the anomalous couplings is enhanced at higher energies. The anomalous couplings can be studied in the processes such as $e^+e^- \to W^+W^-$ and $e^+e^- \to \bar{\nu}W^+e^-$, both of them have large cross sections and are expected to allow us precision measurements. We will return to this point later.

The recent developments of polarized electron sources are quite impressive[2] and worth mentioning here. An electron polarization of more than 80 % has already been achieved and its application to future linear colliders seems promising. We will see later that the polarized electron beam plays an essential role in the studies of gauge boson self-couplings.

The most important new feature of TeV linear collider experiments is probably the possibility of parton identification by jet invariant mass method. At higher energies, jets become jettier and calorimetric energy resolution improves. As we will see later, the identification and the 4-momentum determination of W, Z, and t are therefore relatively easy. By analyzing the angular distributions of daughter partons, we can even measure the helicities of the parents. What we are going to deal with is not a set of a few tens of stable hadrons but a few fundamental particles including light quarks, c, b, t, charged leptons, neutrinos as missing momenta, gluons, photons, W, and Z. Detectors should be able to make full use of this new feature and to allow us to observe Feynman diagrams almost directly.

So far so good. There are, however, some potential problems inherent in TeV linear collider experiments. First of all, we should carefully study the effects of beamstrahlung and finite beam energy spread. Fig.3 shows the luminosity for which the effective center of mass

energy is greater than some fraction, $1-x$, of the maximum possible value, $2E_{beam}^{max}$ in the case of the current JLC design[3]. This example shows that, even in the 1.5 TeV case, more than 40 % of the luminosity is delivered without any beamstrahlung and, if we allow a 10 % loss of the collision energy, the available luminosity increases to more than about 70 % of the total. The beamstrahlung is less significant at 0.5 TeV, where more than 90 % of the luminosity is within 10 % of the maximum center of mass energy. Nevertheless, we should confirm that beamstrahlung and beam energy spread do not harm us too much in event selections and cross section measurements.

Another potential problem is beam-related backgrounds. The beam-related backgrounds can be classified into two groups: i) synchrotron radiations, muons, etc. from beam losses and ii) particles produced during beam-beam interactions. We should prove that we can survive these backgrounds.

Taking into account these new features and our primary physics goal, the quest for L_{Higgs} and L_{Yukawa}, we will discuss the processes shown in Table 1. The table summarizes the representative processes and their relations to our physics goal and the experimental features.

3. Physics Simulation Studies

For simulation studies of the representative processes listed in Table 1, we assume a model detector whose performance is summarized in Table 2. The detector parameters in the table represent those of typical detectors currently working at collider experiments. By the time of the first collision at future linear colliders, we will be able to build a better detector. However, in this talk, we assume a present day technology and see how far we can go.

3.1. Top

Recent results on the top quark mass indicate that

$$91 \text{ GeV} < m_t < 200 \text{ GeV}$$

where the lower limit is from a CDF's analysis while the upper limit is from LEP experiments. These limits imply the following. i) The top is certainly in future linear colliders' reach. ii) Such a heavy top quark opens up a possibility to directly observe top Yukawa interaction. iii) Since the lower limit exceeds the bW threshold, the bW mode will dominate all the other decay channels. This statement is certainly true in the standard model and is also valid in most of its extensions. Therefore, as will be described later, top quarks can be easily identified using the bW mode. iv) Once the bW mode is open, the top width(Γ_t) grows like m_t^3 as shown in Fig.4. For instance, the width is about 1 GeV for $m_t = 150$ GeV and it becomes as large as 2.5 GeV for $m_t = 200$ GeV. Such a large width acts like an infrared cutoff and allows us clean tests of QCD[4]. The large width also prevents top quarks from forming t-hadrons[5]. Therefore the top quarks transfer their spin information to decay daughters. This provides us with a powerful tool to study both decay and production vertices

as we will see later. Another important point is that the top quarks decay predominantly to longitudinal W bosons(see Fig.4), which can be used to study Higgs and Yukawa sectors through loop corrections to the tbW vertex.

Top Quark Productions

There are many ways to produce top quarks at future linear colliders. Among them, the most important are i) $e^+e^- \to t\bar{t}$, ii) $e^+e^- \to t\bar{t}Z$[6], iii) $e^+e^- \to \nu\bar{\nu}t\bar{t}$[7], and iv) $e^+e^- \to t\bar{t}H$[8]. Processes ii) and iii) are very useful to study the Higgs and the Yukawa sectors when the $H \to t\bar{t}$ decay is kinematically allowed, otherwise processes i) and iv) become very important to measure the top Yukawa coupling. Figs.5-a) to -c) show production cross sections for these four processes as a function of $\sqrt{s}$ for three representative top masses: a) $m_t = 100$ GeV, b) $m_t = 150$ GeV, and c) $m_t = 200$ GeV. As we can see, the pair production process has the largest cross section in the energy range of next generation linear colliders. For instance, an integrated luminosity of 10 fb^{-1} at $\sqrt{s} = 500$ GeV yields 5 k $t\bar{t}$ pairs even in the heaviest case of $m_t = 200$ GeV. Therefore, we will focus our attention to the pair production process which involves all the essential features of analysis procedure necessary for top quark studies.

The $t\bar{t}$ pair production cross section[4,9] includes the following parameters:

$$\sigma(\sqrt{s}; m_t, \Gamma_t, \alpha_s(M_Z), M_H, \beta_H)$$

where $\alpha_s(M_Z)$ is the QCD coupling constant, M_H the Higgs mass, and β_H the normalized Yukawa coupling($\beta_H = 1$ for the standard model). Γ_t carries informations on $|V_{tb}|^2$ and new exotic decay modes if any. Figs.6-a) to -d) show the dependence of the threshold shape on these parameters in the case of $m_t = 150$ GeV. As the strong coupling constant gets larger, the QCD potential becomes deeper and consequently the first resonance position shifts down and the threshold enhancement becomes larger. On the other hand, the narrower width gives the higher cross section at the peak while it makes the tail region lower. The Higgs exchange induces an attractive force and its effect becomes more significant as the Higgs mass gets smaller and the Yukawa coupling gets larger. Notice that the shift of the peak postion is less prominent than in Fig.6-a), since the attractive force is short-ranged.

Beam Effects

What we will actually observe is the convolution of the threshold shape presented above and the effective center of mass energy distribution. Fig.7-a) is a JLC example of the effective $\sqrt{s}$ distribution in the presence of beam energy spread and beamstrahlung. The sharp peak at $\sqrt{s_{eff}}/\sqrt{s_0} = 1$(δ-function part) corresponds to the case where no beamstrahlung occurs, while the long tail extending downwards is due to beamstrahlung. The result of the convolution is shown in Fig.7-b), where the threshold shapes before and after the correction for initial state radiations are also plotted for comparison. Notice that the peak smearing is mostly caused by the beam energy spread. The effect of the beamstrahlung is essentially some loss of usable luminosity. This becomes clear when we switch off the beamstrahlung and look at how the threshold shape changes with the beam energy spread. Fig.8-a) plots the reduced center of mass energy distributions for various beam energy widths, where two kinds of spectra, flat-top and double-peak which is more realistic, are compared.

The corresponding threshold shapes are shown in Fig.8-b). As the beam energy spread increases, the first resonance peak quickly disappears. Notice also that the threshold shape depends on the structure insinde the δ-function part. For precision measurements, we need to know the beam energy spectrum with a high resolution.

Event Selection

The signature of $t\bar{t}$ pair productions is two b quarks and two W bosons in the final state. In order to demonstrate the power of the jet invariant method, we will focus our attention to the case where both W bosons decay hadronically. This mode has a branching fraction of about 45 %. Fig.9-a) is a typical 6-jet event expected from this mode. A calorimetric picture of the same event is shown in Fig.9-b) where we can clearly see six jets. The selection of such an event is straightforward. We first demand six jets and require two jet pairs which have invariant masses consistent with M_W. The two 3-jet systems consisting of each W candidate and one of the remaining two jets have to have invariant masses approximately equal to m_t. Finally we impose a cut on thrust to eliminate backgrounds from W pair productions. Fig.10-a) shows a scatter plot of the invariant masses for the two W boson candidates, together with the projections to both axes. We can see clear W boson peaks. The effectiveness of the thrust cut can be seen in Fig.10-b). A signal to background ratio of greater than 10 is easily obtained while keeping the overall detection efficiency reasonable: $\epsilon \simeq 0.26$.

Determinations of Various Parameters

The selected $t\bar{t}$ sample can be used to determine various parameters that enter the cross section formula[10]. Fig.11-a) is an example of energy scan to determine m_t and $\alpha_s(M_Z)$. Each data point corresponds to 1 fb^{-1} and was generated with $m_t = 150$ GeV, $|V_{tb}|^2 = 1$, $\alpha_s(M_Z) = 0.12$, and $M_H = \infty$(no Higgs). The two-parameter fit to these data points results in the contour plot shown in Fig.11-b). The strong correlation between m_t and $\alpha_s(M_Z)$ stems from the fact that the resonance mass decreases as $\alpha_s(M_Z)$ increases. In spite of this strong correlation, we can determine m_t to an accuracy of $\Delta m_t \simeq 0.2$ GeV, even if $\alpha_s(M_Z)$ is totally unconstrained. The significance of the top mass determined this way cannot be underestimated as an input to all sorts of radiative corrections. If the Higgs sector contains more than one doublet, the importance of the top mass will be further enhanced. We can fit the same data points with m_t and Γ_t as free parameters(see Fig.12-a)). The resultant contours are given in Fig.12-b). This time, the correlation between the parameters is very weak. The expected error on the top width is $\Delta\Gamma_t/\Gamma_t \simeq 0.2$. More interesting is the fit to determine β_H(the normalized top Yukawa coupling) and M_H. Figs.13-a) and b) compare the same Monte Carlo data points with threshold curves for various M_H and β_H values. Fig.13-c) shows the contours resulting from the two-parameter fit. In the case of the standard model Higgs($\beta_H = 1$), the energy scan is sensitive to M_H up to about 120 GeV.

In the open top region, we can determine m_t directly from the 3-jet invariant mass. Fig.15 plots the invariant mass for a 3-jet system[11] which consists of a jet pair corresponding to a W boson candidate and a b-jet candidate chosen from the remaining two jets. We can see a clear top quark peak over a broad background coming from wrong combinations. The root mean square width of the peak is about 3.3 GeV which is dominated by detector resolutions. The expected statistical error on the peak position is $\Delta m_t \simeq 0.1$ GeV for 1 k detected top quarks which correspond to an integrated luminosity of about 10 fb^{-1} at $\sqrt{s} = 500$ GeV.

W Polarization from t Decay

As mentioned previously, the heavy top quark decays predominantly to a longitudinally polarized W boson(W_L) which has its origin in the spontaneous symmetry breaking. Therefore the polarization measurement of W's from t decays provides us with opportunities to investigate L_{Higgs} and L_{Yukawa}. For instance, the diagram shown in Fig.14 contains both ttH and WWH couplings which should modify the tree level branching fraction to W_L bosons. Let us now see how well we can determine this branching fraction experimentally. The polarization state of the W boson can be determined by observing the anglular distribution of $W \to q\bar{q'}$ decays in the W's helicity frame. Fig.16-a) plots the cosine of the helicity angle for reconstructed W bosons. The Monte Carlo events were generated with $m_t = 150$ GeV and correspond to an integrated luminosity of 7 fb^{-1} at $\sqrt{s} = 350$ GeV. The solid line superposed in the same figure is the standard model prediction which agrees well with the data points. The tree level branching fraction to W_L bosons and its expected statistical error are shown in Fig.16-b) where the 1-σ bound corresponds to 1 k observed top decays. A data sample of 10 fb^{-1} at $\sqrt{s} = 350$ GeV enables us to determine the branching fraction with a statistical precision of about 2 %.

3.2. *W and Z*

It is well known that the low energy phenomenology resembles that expected from renormalizable gauge theories, even though the underlying theory contains effective higher dimensional couplings. Therefore, there is no reason to blindly believe that weak bosons are truely elementary gauge bosons. Future linear colliders give us possibilities to discover some non-gauge piece of interactions among gauge bosons[12]. In general, CP conserving anomalous triple gauge boson self-couplings[13] can be parameterized as

$$\Delta L_{WWV} \sim \Delta\kappa_V W_\mu^\dagger W_\nu V^{\mu\nu} + \frac{\lambda_V}{M_W^2} W_{\rho\mu}^\dagger W_\nu^\mu V^{\nu\rho}$$

where

$$F^{\mu\nu} \equiv \partial^\mu F^\nu - \partial^\nu F^\mu \quad (F = W/V)$$

and V stands for either γ and Z. In this section, we will examine how well we can determine $\Delta\kappa_V$ and λ_V, using the process: $e^+e^- \to W^+W^-$.

Event Selection

In order to fully make use of the information contained in the differential cross section, we need to identify the charge of the W bosons. For this purpose, we use the final state where one W decays into $q\bar{q'}$ and the other into $l\bar{\nu}$ or $\bar{l}\nu$. Thus we first require an isolated e or μ and the remaining two jets to have an invariant mass consistent with M_W. The 4-momentum of the missing ν is reconstructed by imposing

$$\begin{cases} (p_l + p_\nu)^2 = M_W^2 \\ p_l + p_\nu + p_{q\bar{q'}} = p_{e^+e^-} \\ p_{e^+e^-} = (E_+ + E_-, 0, 0, E_+ - E_-) \end{cases}$$

and

$$p_l^0 + p_\nu^0 + p_{q\bar{q}'}^0 > 0.8 \cdot \sqrt{s}.$$

The overall detection efficiency is about 10 % which includes the branching ratio of 29 % to the final state. Therefore an integrated luminosity of 30 fb^{-1} at $\sqrt{s} = 500$ GeV yields 5 k reconstructed W pair events.

Angular Analysis

The full angular analysis including the W boson decays is non-trivial in the presence of brems- and beamstrahlungs. Here, we will examine how well we can measure the angles involved in this analysis. The relevent angles are the production angle of the W^- boson(Θ), the helicity angle(θ) of the l^- from the W^- decay, that of the l^+($\overline{\theta}$) from the W^+ decay, the azimuthal angle(ϕ) of the W^-'s decay plane measured from its production angle, and that of the W^+'s decay plane($\overline{\phi}$). These angles are depicted in Fig.17. As discussed above, our analysis relies on the reconstruction of the missing neutrino mementum. Given the missing neutrino momentum, we can calculate the effective center of mass energy. Fig.18-a) plots the difference between the reconstructed and generated effective center of mass energy against the generated one. Figs.18-b) to -d) are similar plots for the three angles defined above. The projections of Figs.18-a) to -d) to the vertical axes are shown in Figs.18-e) to -h) which give reasonable resolutions: $\sigma_{\Delta\sqrt{s}} = 20$ GeV, $\sigma_{\Delta\cos\Theta} = 0.023$, $\sigma_{\Delta\cos\theta} = 0.039$, and $\sigma_{\Delta\phi} = 0.054$.

The sensitivity of the angular analysis to the anomalous couplings has been studied by several authors[14,15]. Figs.19-a) to -d) are MIYAMOTO's results assuming an integrated luminosity of 30 fb^{-1} at $\sqrt{s} = 500$ GeV. The dashed curves in the figures represent the expected 90 % confidence level limits for pairs of the anomalous couplings, when the Monte Carlo data for the standard model couplings are fitted to the differential cross section formula:

$$\frac{d\sigma}{d\cos\Theta d\cos\theta d\cos\overline{\theta}},$$

letting the pair of the anomalous couplings in question move freely while keeping the other fixed at the standard model values. Notice that MIYAMOTO included a 5 % systematic error in the fits to be realistic. A beam polarization of 80 % reduces the limits significantly as indicated by the solid curves. In particular, the two-fold ambiguity in Fig.19-a) can be resolved by the measurement of beam polarization asymmetry. The dot-dashed curves are the limits expected from SSC[16]. It should be emphasized that linear collider experiments are indispensable to constrain the $\Delta\kappa$ couplings, though SSC can set similarly stringent limits on the λ couplings. The precision obtainable here is comparable to the expected size of loop corrections.

3.3. Higgs

As stated before, the most important task of future linear colliders is to reveal the structure of the two unknown sectors: L_{Higgs} and L_{Yukawa}. The Higgs boson is at the core of these two sectors and participates in the two important vertices: $VVH \in L_{Higgs}$, where V represents either $W^\pm$ or Z, and $ffH \in L_{Yukawa}$. These two vertices are responsible for productions and decays of the Higgs boson. When $M_H < 2M_W$, the process $e^+e^- \to ZH$ is the best channel to produce the Higgs boson. In this case, the Higgs to $t\bar{t}$ decay is kinematically forbidden and the dominant decay mode is $H \to b\bar{b}$(see Fig.20). In order to study the Yukawa coupling of the top quark, therefore, we need to study the $t\bar{t}$ threshold or the process $e^+e^- \to t\bar{t}H$. Cross sections for these s-channel processes goes like $1/s$ and is not suitable when $M_H > 2M_W$. The W fusion process $e^+e^- \to \nu\bar{\nu}H$, whose cross section behaves like $\log s$, is the channel to use. In Fig.21, the cross sections for $e^+e^- \to ZH$ and $e^+e^- \to \nu\bar{\nu}H$ are given as a function of $\sqrt{s}$ for various Higgs boson masses. A heavy Higgs boson predominantly decays into weak boson pairs: $BR(H \to W^+W^-) \simeq 70$ % and $BR(H \to ZZ) \simeq 30$ %. The $H \to t\bar{t}$ mode may have a branching fraction as large as 10 %, depending on m_t.

It is widely believed that the Higgs hunting at future linear colliders will be easy if $2M_W < M_H \lesssim 0.5$ GeV, since, in this case, we can use the $H \to W^+W^-$ mode, which should be easily identified by reconstructing the W bosons via jet invariant mass method and by looking for a mass peak in the WW invariant mass distribution. Unlike at hadron colliders, the $M_Z < M_H < 2M_W$ case is also relatively easy to handle, since the 4-jet final state from $e^+e^- \to ZH$ can also be reconstructed by the jet invariant mass method. Thus two difficult cases remain: i) $M_H \simeq M_Z$ and ii) $M_H \gtrsim 0.5$ GeV. In the latter case, the width of the Higgs boson grows like $\Gamma_H \simeq 0.5 \cdot M_H(\text{TeV})^3$ and the peak hunting becomes nontrivial. In what follows, let us see how we can treat these two difficult cases.

$M_H = M_Z$

The potential backgrounds to the process $e^+e^- \to ZH$ are $e^+e^- \to W^+W^-$ and $e^+e^- \to ZZ$. The WW background, which has the largest cross section, can be eliminated by requiring a lepton pair whose invariant mass is consistent with M_Z. Now the question is how to suppress the ZZ background. Apparently, the use of vertex detector is very effective, since the Higgs in question predominantly decays into $b\bar{b}$, while the ZZ background will be suppressed by the factor $2 \cdot BR(Z \to b\bar{b})$. The cut on the production angle of the Z boson is also effective, since the Z from the ZZ background has forward and backward peaks while the Z from the signal process does not. There is yet another way. Notice that the Z boson from the ZH final state has a longitudinal polarization. The Z from the ZZ background, on the other hand, is transversely polarized. This difference results in the different helicity angle distributions for the leptons from Z decays: $Z_L \to l^+l^-$ behaves like $\sin^2\theta_l^*$ while $Z_T \to l^+l^-$ like $1 + \cos^2\theta_l^*$. We can use a projection operator to project out events with longitudinal Z bosons.

KANZAKI[17] took this approach. His event selection looks for events with a pair of electrons, whose invariant mass is roughly equal to M_Z, and additional two jets. The magnitudes of their 4-momenta can be corrected to improve invariant mass resolution, thanks to the precisely known 4-momenta of the two leptons. The cut on the Z's production angle,

$|\cos\theta_Z| < 0.6$, enhances the signal by rejecting the ZZ background in the forward and backward regions.

The detection efficiency for the ZH final state is about 0.01 including the branching fractions: $BR(H \to q\bar{q}) = 0.95$ and $BR(Z \to e^+e^-) = 0.03$. About 30 ZH events are expected for 30 fb^{-1} at $\sqrt{s} = 0.5$ TeV. Surely we can use the $Z \to \mu^+\mu^-$ mode which doubles the expected statistics.

Fig.22-a) shows the invariant mass distribution of the two jet system before applying the projection operator. Even in this stage, the excess of events is statistically significant. The effect of the projection operator can be seen in Fig.22-b) where we can see a clear peak from the Higgs boson production.

$M_H \gtrsim 0.5$ TeV

In this subsection, we will discuss searches for a heavy Higgs boson via the WW fusion process: $e^+e^- \to \nu\bar{\nu}H$ with a subsequent decay of $H \to W^+W^-$. Here we will focus our attention to 4-jet final states where both of the W bosons decay hadronically. The main background to this process comes from $e^+e^- \to e^+e^-W^+W^-$. This background can be significantly reduced by vetoing $e^\pm$ and imposing a cut on the transverse momentum of the WW system. We will see how this works by taking examples of KURIHARA's studies[18].

KURIHARA first requires two pairs of 2-jet systems which have invariant masses consistent with M_W and then vetoes $e^\pm$'s with $\theta_e > 150$ mrad and $E_e > 50$ GeV. Finally he demands $p_T^{WW} > 0.08 \cdot E_{beam}$. The expected detection efficiency after these cuts is 0.16 including the branching fraction factor: $BR(W \to q\bar{q}')^2 = 0.45$.

Fig.23 shows the imvariant mass distribution for the WW system for $M_H = 0.5$ TeV and an integrated luminosity of 60 fb^{-1} at $\sqrt{s} = 1.0$ TeV. A clear peak from Higgs boson productions stands out over the background. When the Higgs mass becomes larger, the search will be more difficult. In the case of $M_H = 1.0$ TeV, we can not expect to observe a clear mass peak any more. Instead, what we will see is a broad enhancement. We should be careful, when we estimate the enhancement, since the naive use of the tree amplitudes with $M_H = 1.0$ TeV violates the unitarity of the $J = 0$ $I = 0$ partial wave in the presence of non-Higgs diagrams. This is shown in Fig.24-a). KURIHARA avoids this by enlarging the Higgs width as in Fig.24-b). Fig.25 compares the WW invariant mass distribution for $M_H = 1.0$ TeV with that for $M_H = 0$. An accumulation of 130 fb^{-1} at $\sqrt{s} = 1.5$ TeV gives us a 3-σ enhancement over the $M_H = 0$ case.

WW Rescattering

The Higgs sector enters a strongly interacting regime when the Higgs mass increases further. Such a case can be studied by investigating the final state interaction of the WW system produced in the process: $e^+e^- \to W^+W^-$(see Fig.26). The rescattering takes place between the longitudinal W bosons and modifies the helicity amplitude T_{LL}. The effect of this rescattering gives rise to a phase shift: $T_{LL} \to T_{LL} \cdot e^{i\delta}$ where δ has been calculated by HIKASA[19] as

$$\delta = \frac{G_F}{48\sqrt{2}\pi} \cdot s$$

which is valid when $M_W^2 \ll s \ll M_H^2$. The phase shift δ is about 0.1 radian at $\sqrt{s} = 1.5$ TeV

which should be obervable through the T_{LL}-T_{TT} interference.

MIYAMOTO[20,19,15] studied how well we can determine this phase shift by performing an angular analysis we discussed before. Fig.27 compares the correlations between the azimuthal angles defined in Fig.17 for $\delta = 0$ and $\delta = 0.1$, where the following cuts are implicit which enhance the sensitivity to the phase shift:

$$-1 < \cos\Theta < 0.5$$

$$|\cos\theta|, |\cos\bar{\theta}| < 0.9.$$

The points with error bars in the figure correspond to 1k reconstructed WW events. In order to quantify the sensitivity to the phase shift, Fig.28 shows the 90 % confidence limit on δ as a function of the number of detected W^+W^- events, when the Monte Carlo events are generated with $\delta = 0$. Given a sample of 800 reconstructed events at $\sqrt{s} = 1.5$ TeV, we may start observing the expected phase shift for the strongly interacting Higgs sector. Considering the effective cross section including the geometrical acceptance, $\sigma_{eff} = 52$ fb, the required statistics seems feasible, although we must study more carefully about the charge ID efficiency of the decay daughters.

BARKLOW[15] performed a similar analysis with a different parametrization of the modification factor: $T_{LL} \to F_T \cdot T_{LL}$ where

$$F_T \equiv \frac{M_{\rho_{TC}}^2 - iM_{\rho_{TC}}\Gamma_{\rho_{TC}}}{M_{\rho_{TC}}^2 - s - iM_{\rho_{TC}}\Gamma_{\rho_{TC}}},$$

assuming a ρ-like resonance. The 95 % confidence level bounds in the complex F_T plane is depicted in Fig.29 for an integrated luminosity of 200 fb^{-1} at $\sqrt{s} = 1.0$ TeV. The figure tells us that a techni-ρ with a mass as large as 3 TeV can be easily detected, though the low energy theorem case(LET) requires more statistics or higher energy to observe.

4. Backgrounds

As stated before, there are two classes of beam-related backgrounds. The first class consists of those backgrounds which originate from beam losses. Wake fields, secondary scatters from slits, beam-gas interactions, compton scattering, and bremsstrahlung create beam tails which may hit final focus apertures and slits and produce secondary particles such as muons, electrons, and photons. The beam tails also induce synchrotron radiations. These beam-related backgrounds are severer at linear colliders than those at storage ring machines, since the beam tails are renewed on every beam crossing. The backgrounds due to beam-beam interactions are new and peculiar to linear colliders and comprise the second class. In order to protect ourselves from these two kinds of backgrounds, we have to carefully design the interaction region. Fig.30 shows an example of JLC IP layouts[21]. We will see below how this works.

4.1. *Backgrounds from Beam Losses*

Synchrotron Radiations

The synchrotron radiations from beam tails are potentially one of the most serious backgrounds. TAUCHI[22] performed systematic studies on the synchrotron radiation background, based on the current JLC final focus design. The JLC mask system shown in Fig.30 has a geometrical acceptance of $\simeq 10^{-3}$ for a photon back-scattered from the final quadrupole front face. Taking into account the probability of back scattering of $\simeq 10^{-2}$ and the photon-to-electron conversion efficiency of $\simeq 10^{-2}$ in gas chambers, the acceptable limit is somewhere around 10^8 photons hitting the final quadupole. Figs.31-a) and -b) show the number of photons with energies greater than 10 KeV as a function of the horizontal and vertical distances from IP, respectively. The horizontal lines in the figure indicate the above mentioned upper limit. Apparently, if the beam profile were Gaussian(no beam tail) this background would be absent, since the half aperture of the final quadrupole is 2.5 mm. Even in the presence of a non-Gaussian beam tail, we can eliminate the synchrotron background with a properly designed collimeter to cut out the beam tail at, say, 10-σ.

Muons

The experience at SLC taught us that we should watch out muon backgrounds produced far-upstream in the beam line. Fig.32, which is a SLC example[23], demonstrates the effect of troidal magnets to sweep out the muon backgrounds. Without the muon spoiler(see the upper histogram), some 10's of muons reach the detector, while with the spoiler(see the lower figure), the muon background can be suppresed to a tolerable level.

4.2. *Backgrounds due to Beam-Beam Interactions*

Beam-Beam Pair Productions

It is now widely known that e^+e^- pairs produced in beam-beam interactions would polute the whole IP region and might hamper otherwise available detector performance, if the design criteria for the IP layout and the machine itself did not include this background from the beginning. The major sources of the e^+e^- pairs are the following three incoherent processes: a) $e^+e^- \to e^+e^-e^+e^-$, b) $\gamma \to e^+e^-e$, and c) $\gamma\gamma \to e^+e^-$, where photons come from beamstrahlung. The use of flat beam optics reduces significantly the beamstrahlung and its conversion into e^+e^- pairs by the strong electric field produced by the opposing beam, the so called coherent process[24] which comprises yet another source of e^+e^- pairs. The dominant background source now becomes process a). Although the flat beam does not suppress the event rate for process a), it reduces the fraction of electrons and positrons that hit the final quadrupole front face, since the electromagnetic field produced by the opposing beam which gives transverse kick decreases considerably. Nevertheless, it is non-trivial whether we should make the beam crossing angle large($\gtrsim$ 30 mrad) and prevent the most of e^+e^- pairs from hitting the final quadrupole, or we may keep the crossing angle small($\simeq$ 5 mrad) and let them hit the quadrupole. In the latter case, we need, of course, a proper shielding. From the machine construction point of view, the latter option is preferable, since the former requires crab-crossing. TAUCHI, YOKOYA, and CHEN[25] calculated the integrated number of pair-produced electrons or positrons during a single bunch crossing

as a function of P_T^{min} which is plotted in Fig.33. The electrons or positrons hitting the final quadupole yield one popping-out photon, on average, as a result of the annihilations of positrons produced in electromagnetic showers. It is thus very important to mask the photons from the pair-produced electrons and positrons populating the low P_T bumps in the figure. The mask system shown in Fig.30 can shield the 0.5 MeV photons, provided that the minimum inner radius of the mask is large enough to let the low P_T electrons and positrons curl into the mask system, in a magnetic field of 2 T.

Photon-Induced Hadronic Background

DREES[26] pointed out that there is yet another potential background induced by beam-beam interactions. The so called mini-jet events stem from the interactions of hadronic components inside photons. Figs.34-a) to -c) depict three mechanisms to produce hadronic backgrounds. The first(Fig.34-a)) is the well known direct two-photon process. Fig.34-b) and -c) are the new sources of hadronic backgounds, where the hadronic structures of photons are resolved. The rate of these mini-jet events is not suppressed by powers of α_s, because of collinear singularity, and increases with beam energy. As a result, the photon-photon interaction becomes somewhat similar to hadron-hadron interactions. Beamstrahlung photons also participate in these mini-jet processes. If the mini-jet rate is high, the virtue of e^+e^- collider might be lost. Here again, the use of flat beam helps greatly, since it reduces the number of beamsthrahlung photons. The three kinds of processes shown in Figs.34-a) to -c) are, however, not affected. MIYAMOTO[27] carried out simulation studies on this. Fig.35-a) is an example of Monte Carlo mini-jet events where the bottom figure is a calorimetric view of the same event. At $\sqrt{s} = 500$ GeV, the rate of such events is one per train crossing in the case of the current JLC design. The mini-jet event in Fig.35-a) should be compared with, for instance, the W^+W^- event in Fig.35-b) taken as a representative of signal events. From these two figures we may conclude that the mini-jet events will not trouble us too much. Those who are not convinced by this should work out some method to separate mini-jet tracks. BURKE proposes to decide which track belongs to which bunch on a track by track basis, making use of t_0 information provided by the central drift chamber. When the t_0, the timing corresponding to zero drift length, is wrong, the track segments measured in adjacent staggered cells do not match at their boundary. Requiring these track segments meet at each boundary determines t_0. Fig.36[28] shows a MARK-II(SLC) example of the so determined t_0 distribution. The standard deviation of the distribution is 1.4 nsec which is comparable to a typical bunch spacing(20 bunches spaced by every 1.4 nsec for the current JLC design). If we include the t_0 measurement to the design criteria for the central tracker, it should be possible to get $\sigma_{t_0} \lesssim 0.5$ nsec.

5. Summary and Conclusion

Next generation e^+e^- collider experiments have many unique features. In particular, the parton identification and 4-momentum and spin measurements via jet reconstruction will be a powerful tool to extract detailed informations.

For example, top mass can be determined with a precision $\sigma_{m_t} \lesssim 0.5$ GeV through both threshold scan and jet reconstruction, if an integrated luminosity of $\gtrsim 10$ fb^{-1} is given. The same integrated luminosity allows us to measure top Yukawa coupling for $M_H \lesssim 100$ GeV. We have demonstrated that this kind of precision can be achieved even under the $\sqrt{s}$ smearing due to beam energy spread and beamstrahlung.

With an integrated luminosity in excess of 30 fb^{-1} at $\sqrt{s} = 500$ GeV, we can squeeze the limit on the anomalous coupling($\Delta\kappa$ and λ) down to 0.02 which is comparable to the expected size of loop corrections. The polarized electron beam and angular analysis based on jet reconstruction will play a crucial role here. It should be emphasized that the $\Delta\kappa$ measurent requires a linear collider, though hadron colliders such as SSC and LHC can measure the λ coupling with a similar precision.

As for Higgs hunting, two difficult cases were examined. In the first case where $M_H = M_Z$, an integrated luminosity of $\gtrsim 30$ fb^{-1} at $\sqrt{s} = 500$ GeV is enough to separate the Higgs signal from the ZZ background, using the process $e^+e^- \to ZH$ and the Z and H decaying into lepton pairs and quark pairs, respectively. The second case considered is a 1 TeV Higgs. The width of such a heavy Higgs becomes comparable to its mass and we can no longer expect to see any clear mass peak in the WW invariant mass distribution. Nevertheless, we can see a 3-σ signal if an integrated luminosity in excess of 100 fb^{-1} at 1.5 TeV(1 JLC year for the current JLC design) is available. Such a high luminosity allows us to study the strongly interacting Higgs sector, if any, by studying the longitudinal W rescattering in the process $e^+e^- \to W^+W^-$. For instance, an integrated luminosity of $\gtrsim 300$ fb^{-1} at $\sqrt{s} = 1.5$ TeV enables us to detect the LET case.

The background problems including e^+e^- pairs and mini-jet events induced by beam-beam interactions can be tamed and made consistent with the currently considered designs of next generation linear colliders.

In conclusion, the physics potential of a 0.5 TeV linear collider is comparable and, in many respects, complementary to future hadron colliders such as SSC and LHC. When the center of mass energy reaches 1.0 to 1.5 TeV eventually, its potential may surpass that of SSC and LHC.

Acknowledgements:

The author wishes to thank all the members of the JLC physics working group. The most of the materials presented here are due to their enthusiastic efforts. He is also grateful to Prof. M. S. Chanowitz for valuable discussions. Finally, the author would like to express his heartfelt gratitude to the conference organizers for making this conference so comfortable and so successful.

REFERENCES

1. Characteristic features of e^+e^- collider experiments were also discussed by M. S. Chanowitz, these proceedings.
2. T. Nakanishi, et al., *KEK Preprint* 91-51 (1991).
3. K. Yokoya, plenary talk given at *Workshop on Physics and Experiments with Linear Colliders*, Saariselkä, Finland, September (1991).
4. V. Fadin and V. Khoze, *Sov. J. Nucl. Phys.* **48** (1988) 309.
5. J. Kühn, *Acta Physica Austriaca, Suppl.* **XXIV** (1982) 203, I. Bigi, Y. Dokshitzer, V. Khoze, J. Kühn, and P. Zerwas, *Phys. Lett.*, **B181** (1986) 157.
6. K. Hagiwara, H. Murayama, and I. Watanabe, *KEK Preprint* 90-125 (1990), T. Tauchi, K. Fujii, and A. Miyamoto, *KEK Preprint* 90-148 (1990).
7. T. Tsukamoto, *KEK Preprint* 91-17 (1991).
8. A. Djouadi, J. Kalinowski, and P. Zerwas, DESY 91-104.
9. W. Kwong, *Phys. Rev.* **D43** (1991) 1488, M. Strassler and M. Peskin, *Phys. Rev.* **D43** (1991) 1500, Y. Sumino, K. Fujii, K. Hagiwara, H. Murayama, and C.-K. Ng, *KEK Preprint* 91-6 (1991).
10. S. Komamiya, SLAC-PUB-5324 (1991), K. Fujii, *KEK Preprint* 90-187 (1991), K. Fujii, *KEK Preprint* 92-6 (1992).
11. P. Igo-kemenes, private communication.
12. K. Hagiwara, *KEK Preprint* 91-215 (1991).
13. K. Hagiwara, R. D. Peccei, D. Zeppenfeld, and K. Hikasa, *Nucl. Phys.* **B282** (1987) 253.
14. E. Yuhudai, *Phys. Rev.* **D41** (1990) 33, A. Miyamoto, *KEK Preprint* 90-188 (1991).
15. T. L. Barklow, plenary talk given at *Workshop on Physics and Experiments with Linear Colliders*, Saariselkä, Finland, September (1991).
16. G. L. Kane, J. Vidal, and C.-P. Yuan, *Phys. Rev.* **D39** (1990) 2617.
17. J. Kanzaki, *Proceedings of Second JLC Workshop* (1990).
18. Y. Kurihara, *Proceedings of Second JLC Workshop* (1990).
19. K. Hikasa, *KEK Preprint* 91-214 (1992).
20. A. Miyamoto, talk given at *Workshop on Physics and Experiments with Linear Colliders*, Saariselkä, Finland, September (1991).
21. T. Tauchi and T. Matsui, private communication.
22. T. Tauchi, et al., *KEK Preprint* 90-181 (1991).
23. D. Burke, plenary talk given at *Workshop on Physics and Experiments with Linear Colliders*, Saariselkä, Finland, September (1991). For the expected muon background and its possible cure, see L. P. Keller, *SLAC-PUB*-5652 (1991).
24. P. Chen and V. I. Telnov, *SLAC-PUB*-4923 (1989).
25. T. Tauchi, K. Yokoya, and P. Chen, *SLAC-PUB*-5557 (1991).

26. M. Drees and R. M. Godbole, *Phys. Rev. Lett.* **67** (1991) 1189.
27. A. Miyamoto, private communication.
28. C. Adolphsen and D. Burke, private communication.

TABLE CAPTIONS

1: A table summarizing physics and experimental features for representative processes discussed in the text.

2: The parameters of our model detector used in the simulation studies described in the text.

FIGURE CAPTIONS

1) Total cross sections for major standard model processes as a function of $\sqrt{s}$.

2) (a) Lighter chargino mass contours in the plane of the $SU(2)$ gaugino mass M_2 and the higgsino mixing mass μ for $\tan\beta \equiv v_2/v_1 = 10$. The right vertical axis is the corresponding gluino mass. Dotted line is the expected sensitivity limit for SSC and LHC. (b) Scalar fermion mass contours in the plane of M_2 and the common scalar mass m_0 for $\tan\beta = 10$ and $\mu = 4M_W$. Solid lines are for scalar leptons and dashed lines for scalar quarks. Again the dotted line represents the expected sensitivity limit for SSC and LHC.

3) The fraction of the luminosity corresponding to collision energy greater than $\sqrt{s_{coll}}$ in the presence of beam energy spread and beamstrahlung, as a function of fractional energy measured from the nominal center of mass energies: $\sqrt{s}$ = 0.5 TeV(solid), 1.0 TeV(long dash), and 1.5 TeV(short dash).

4) Top quark width as a function of top mass.

5) Total cross sections for $t\bar{t}$, $t\bar{t}Z$, $\nu\bar{\nu}t\bar{t}$, and $t\bar{t}H$ productions for three representative top masses: (a) $m_t = 100$ GeV, (b) $m_t = 150$ GeV, and (c) $m_t = 200$ GeV.

6) The dependence of the $t\bar{t}$ threshold shape for $m_t = 150$ GeV on (a) $\alpha_s(M_Z)$, (b) $\Gamma_t/\Gamma_t(\mathrm{SM};|V_{tb}|^2 = 1)$, (c) M_H assuming $\beta_H^2 = 1$, and (d) β_H^2 for $M_H = 100$ GeV, where β_H is the normalized top Yukawa coupling($\beta_H^2 = 1$ in the standard model).

7) (a) The effective center of mass energy distribution in the presence of beam energy spread and beamstrahlung. (b) Threshold shapes before and after the inculsion of beam energy spread and beamstrahlung.

8) (a) The reduced center of mass energy distributions including the effects of initial state radiations and natural beam energy spread but leaving out the effect of beamstrahlung. Distributions for two kinds of spectra, flat-top and double-peaked which is more realistic, are shown for various beam energy spreads. (b) Corresponding threshold shapes.

9) (a) A typical 6-jet event from $e^+e^- \to t\bar{t} \to bW^+\bar{b}W^-$ where both W^+ and W^- decay into $q\bar{q}$. (b) The same event in the calorimeter.

10) (a) A scatter plot of the invariant masses of the 2-jet systems reconstructed as W boson candidates together with their projection to each axis. (b) Thrust distributions for the $t\bar{t}$ signal and the W^+W^- background with all but the thrust cut indicated by an arrow.

11) (a) An example of energy scan to determine m_t and $\alpha_s(M_Z)$ where each point corresponds to 1 fb^{-1}. (b) The contour resulting from the fit to the data points.

12) (a) An example of energy scan to determine m_t and $|V_{tb}|^2$ where each point corresponds to 1 fb^{-1}. (b) The contour resulting from the fit to the data points.

13) (a) An example of energy scan to determine M_H and β_H^2 where the effective cross section curves are superimposed for several M_H values. (b) The same plot with the effective cross section curves for several β_H^2 values. (c) The contour resulting from the fit to the data points.

14) A 1-loop diagram in the standard model which contains both the Higgs and the Yukawa couplings.

15) Invariant mass distribution for the 3-jet system resulting from $t \to bW$ decays.

16) (a) Helicity angle of q or $\bar{q}$ from W decay. (b) Branching fraction of the $t \to bW_L$ decay as a function of m_t. The dashed curves indicate 1-σ boundaries expected for 1k top decays.

17) Definitions of angles used in the angular analysis of W^+W^- pair productions.

18) (a) The difference between reconstructed and generated $\sqrt{s}$ plotted against the generated $\sqrt{s}$, where the generated $\sqrt{s}$ means the effective center of mass energy after beamstrahlung and initial state radiation. The nominal $\sqrt{s}$ is 500 GeV. (b)-(d) Similar plots for the three angles defined in Fig.17. (e)-(h) Projections of (a) to (d) to the vertical axes, respectively.

19) The expected 90 % confidence level limits on pairs of anomalous self-couplings for an integrated luminosity of 30 fb^{-1} at $\sqrt{s} = 500$ GeV. (a) $\Delta\kappa_\gamma$ and λ_γ. (b) $\Delta\kappa_Z$ and λ_Z. (c) $\Delta\kappa_\gamma$ and $\Delta\kappa_Z$. (d) λ_γ and λ_Z. The vertical cross symbols indicate the standard model positions used as inputs. Solid and dashed lines are with and without using 80 %-polarized electron beam. Dot-dashed lines corresponds to expected SSC limits.

20) Branching fractions of the standard model Higgs boson to various decay modes as a function of the Higgs mass.

21) Total cross sections for the standard model Higgs productions via $e^+e^- \to ZH$(solid lines) and $e^+e^- \to \nu\bar{\nu}H$(dashed lines) as a function of $\sqrt{s}$. The dotted line is the point-like cross section. The numbers in the figure indicate the Higgs mass.

22) The invariant mass distributions of the jet-jet system from the processes: $e^+e^- \to ZZ$(open histograms) and $e^+e^- \to ZH$(hatched part) (a) before and (b) after projecting out $J = 0$ components.

23) The invariant mass distribution of the W^+W^- system originating from $e^+e^- \to \nu\bar{\nu}W^+W^-$, $e^+e^-W^+W^-$, and W^+W^- with initial state radiations and/or beamstrahlungs. The Monte Carlo data points correspond to 60 fb^{-1} at $\sqrt{s} = 1$ TeV. The input Higgs mass is 0.5 TeV.

24) Argand plots for the $J = 0$ $I = 0$ tree-level amplitudes for vector boson elastic scattering (a) with the tree-level Higgs width and (b) with the adjusted Higgs width to avoid unitarity violation. The input Higgs mass is 1 TeV.

25) The invariant mass distributions of the W^+W^- system at $\sqrt{s} = 1.5$ TeV, assuming an integrated luminosity of 130 fb^{-1}. The Monte Carlo data points correspond to the $M_H = 1$ TeV case, while the histogram to the $M_H = 0$ case. Background contributions in the region 0.5 TeV $< M_{WW} <$ 1.0 TeV consist of 6 events from $\nu\overline{\nu}ZZ$, 20 events from $e^{\pm}\nu W^{\mp}Z$, 0 event from $e^+e^-W^+W^-$, and 69 events from W^+W^- with either initial state radiations or beamstrahlungs or both. In the same region the 1 TeV Higgs case gives 183 ± 14 together with the backgrounds, which should be compared with 140 events expected for the zero mass Higgs.

26) The Feynman diagram representing the rescattering of pair produced longitudinal W bosons.

27) The expected correlations between the azimuthal angles defined in Fig.17. The solid line is for $\delta = 0.1$, while the dashed line is for $\delta = 0$. The Monte Carlo data points correspond to 1 k reconstructed W^+W^- events. After the cuts on the angles described in the text, the effective cross section is $\sigma = 52$ fb at $\sqrt{s} = 1.5$ TeV.

28) The expected 90 % confidence level limit on the phase shift from the $d\sigma/d(\phi + \overline{\phi})$ measurement for W_LW_L rescattering as a function of the number of reconstructed W^+W^- events. The input Monte Carlo events were generated with $\delta = 0$. The three dotted lines are the standard model predictions for three representative energies: $\sqrt{s} = 1.0$, 1.5, and 2.0 TeV. In the same figure, the corresponding effective cross sections, which include the geometrical acceptance factor due to the angle cuts, are shown.

29) The expected 95 % confidence level limits on the form factor F_T(see the text) for an integrated luminosity of 200 fb^{-1} at $\sqrt{s} = 1$ TeV, when the input Higgs is light and weakly interacting. The open circles in the figure represents typical scinarios: light Higgs, low energy theorem(LET), and techni-ρ.

30) A sketch of the current JLC IP layout optimized for experiments at $\sqrt{s} = 1$ TeV which shows the configuration of the mask system, the compensation solenoid, and the final quadrupole magnets. The final quadrupole has a bore radius of 2.5 mm and a beam exit hole of > 6 mmϕ.

31) The numbers of synchrotron-radiated photons at IP as a function of (a) horizontal and (b) vertical distances from the beam line, assuming the current JLC optics. Corresponding to three representative beam profiles, three curves are drawn which should be compared with the upper limit indicated in the same figure for the current JLCdesign.

32) The probability of an intercepted electron or positron producing a muon reaching the detector measured at SLC (a) without and (b) with troidal magnets to sweep out muons.

33) The numbers of electrons(positrons) produced per bunch crossing with transverse momenta greater than P_T^{min}. The calculation assumes the current design parameters of three phases of the JLC.

34) Production mechanisms for photon-induced hadronic backgrounds: (a) direct two-photon processes, (b) processes where the hadronic components of one of the two photons are resolved, and c) processes where the hadronic structures of both of them are resolved.

35) (a) An example of mini-jet events expected at the JLC of $\sqrt{s} = 0.5$ TeV. The bottom figure is its calorimetric picture. (b) A similar figures for W pair events.

36) The t_0 distribution measured, on a track by track basis, using MARK-II at SLC.

	Channel	Physics Aim	Experimental Features				
			Parton ID via jet analysis	Angular analysis	Beamstrahlung	E_{BM} spread	Pol-e
Top	$e^+e^- \to t\bar{t}$	$\mathcal{L}_{\text{Yukawa}}$ $(m_t, \Gamma_t, M_H, \beta_H)$	○	○	○	◎	
W/Z	$e^+e^- \to W^+W^-$	Anomalous couplings $(\Delta\kappa, \lambda)$	○	○	○		◎
Higgs	$e^+e^- \to ZH$	$\mathcal{L}_{\text{Higgs}}$ $M_H < 2M_W$	○	◎	○		
	$e^+e^- \to \nu\bar{\nu}H$	$\mathcal{L}_{\text{Higgs}}$ $M_H > 2M_W$	○		○		
	$e^+e^- \to W^+W^-$ Rescattering	$\mathcal{L}_{\text{Higgs}}$ Strong H sector	○	◎	○		

Table 1

		Model Detector Performance
Calorimetry	EM	$\frac{\sigma_E}{E} = \sqrt{\left(\frac{0.1}{\sqrt{E(\text{GeV})}}\right)^2 + (0.02)^2}$ $\Delta\theta = \Delta\phi = 15\text{mrad}$
	Had.	$\frac{\sigma_E}{E} = \sqrt{\left(\frac{0.5}{\sqrt{E(\text{GeV})}}\right)^2 + (0.02)^2}$ $\Delta\theta = \Delta\phi = 50\text{mrad}$
Tracking		$\frac{\sigma_{P_T}}{P_T} = 6 \times 10^{-4} \cdot P_T(\text{GeV})$ $B = 1.5T$
Angular Coverage		Hermetic down to $\theta = 150$ mrad

Table 2

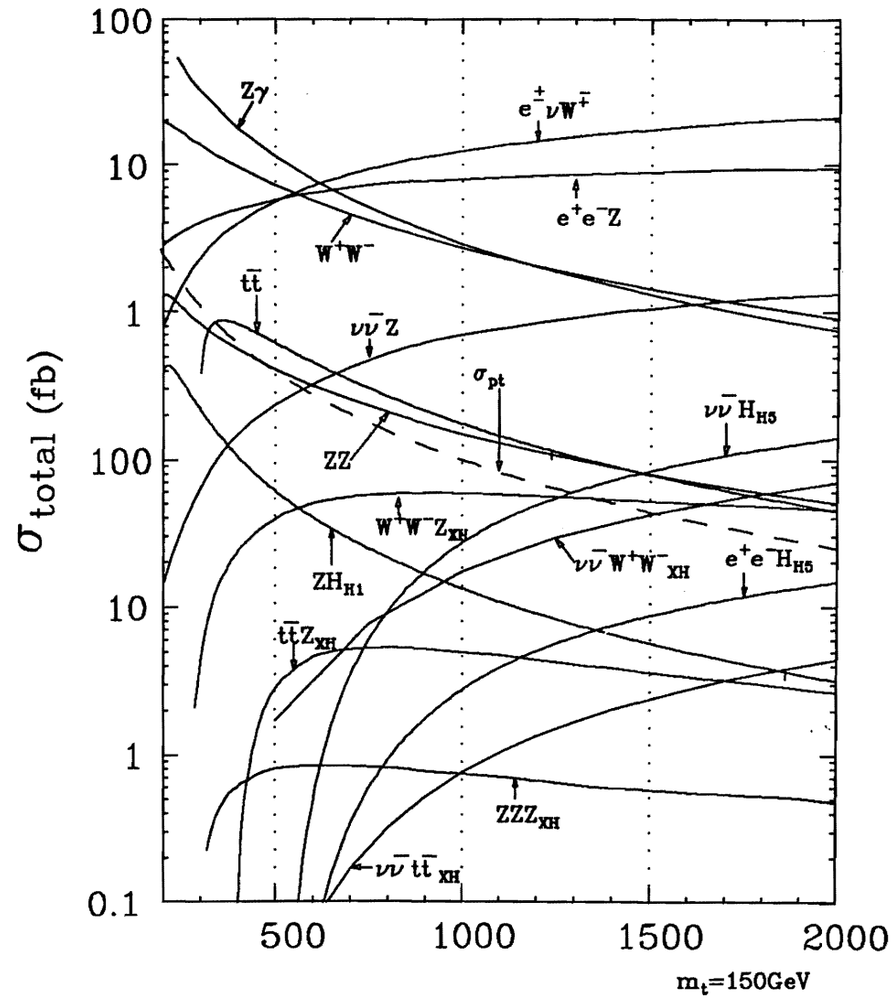

m_t=150GeV
XH : without Higgs
H1 : m_H=100GeV
H5 : m_H=500GeV
No QCD corrections

Fig.1

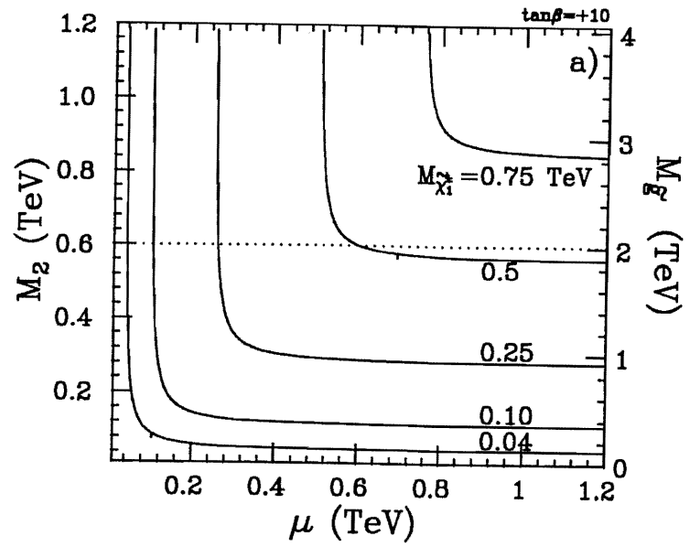

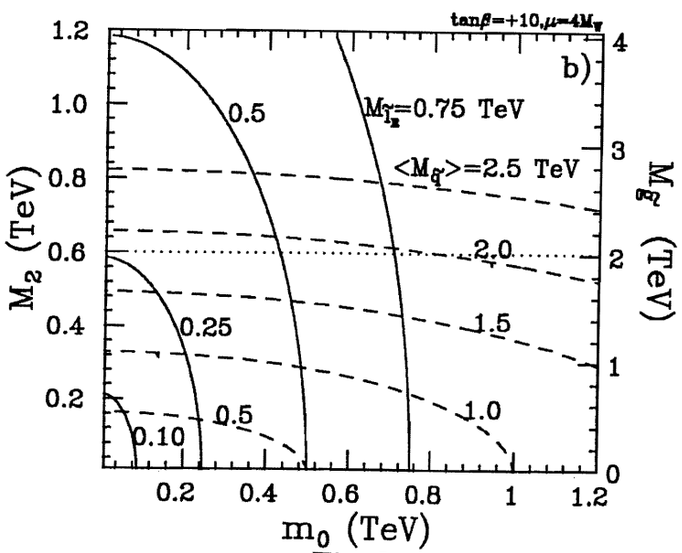

Fig.2

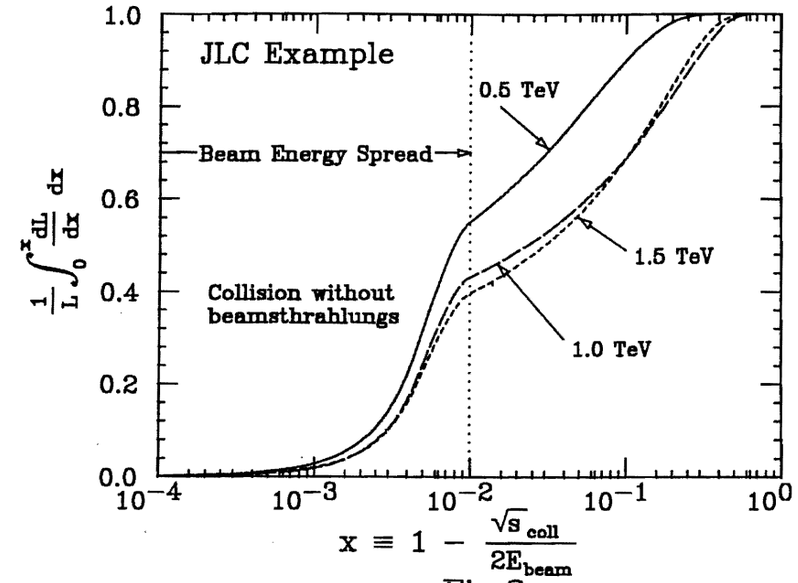

Fig.3

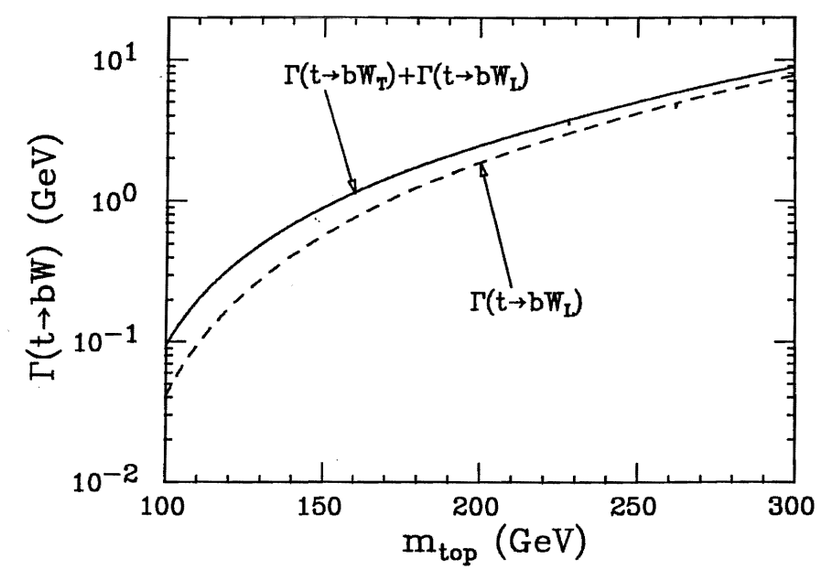

Fig.4

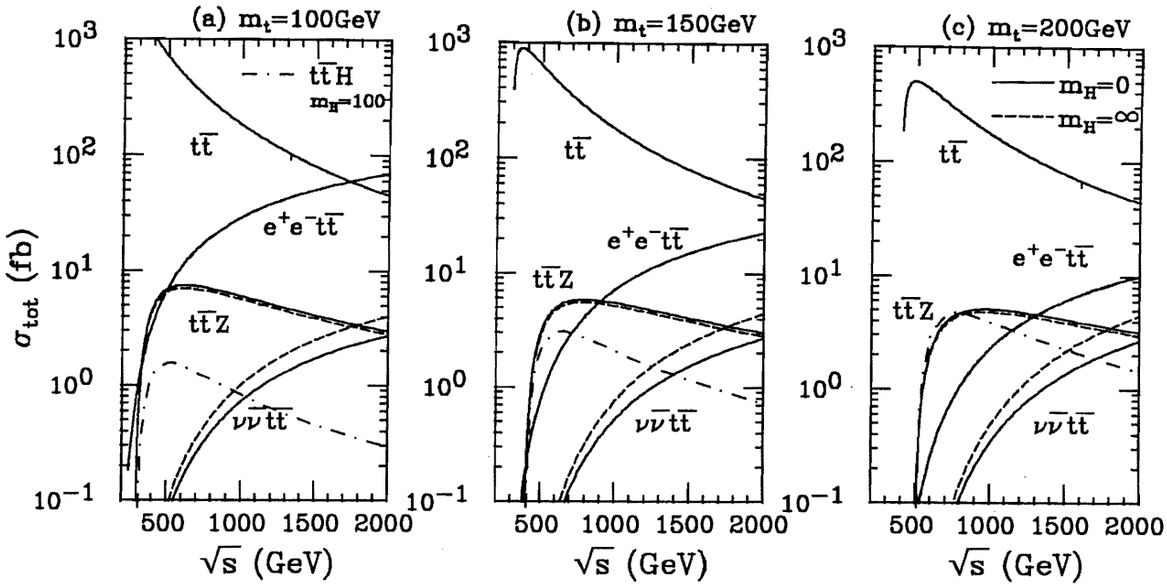
(a) m_t=100GeV
(b) m_t=150GeV
(c) m_t=200GeV
σ_{tot} (fb)
$\sqrt{s}$ (GeV)
$t\bar{t}H$
m_H=100
$t\bar{t}$
$e^+e^-t\bar{t}$
$t\bar{t}Z$
$\nu\bar{\nu}t\bar{t}$
m_H=0
m_H=∞

Fig.5

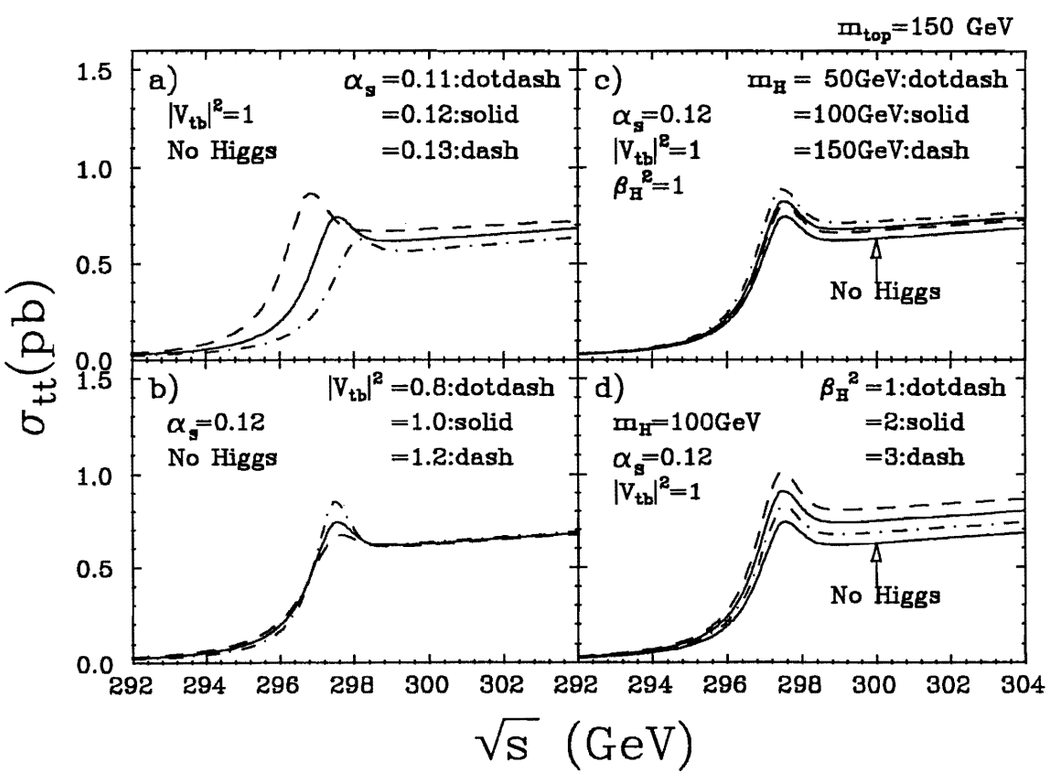
m_{top}=150 GeV
a)
α_s =0.11:dotdash
=0.12:solid
=0.13:dash
$|V_{tb}|^2$=1
No Higgs
b)
$|V_{tb}|^2$ =0.8:dotdash
=1.0:solid
=1.2:dash
α_s=0.12
No Higgs
c)
m_H = 50GeV:dotdash
=100GeV:solid
=150GeV:dash
α_s=0.12
$|V_{tb}|^2$=1
β_H^2=1
No Higgs
d)
β_H^2 =1:dotdash
=2:solid
=3:dash
m_H=100GeV
α_s=0.12
$|V_{tb}|^2$=1
No Higgs
σ_{tt}(pb)
$\sqrt{s}$ (GeV)

Fig.6

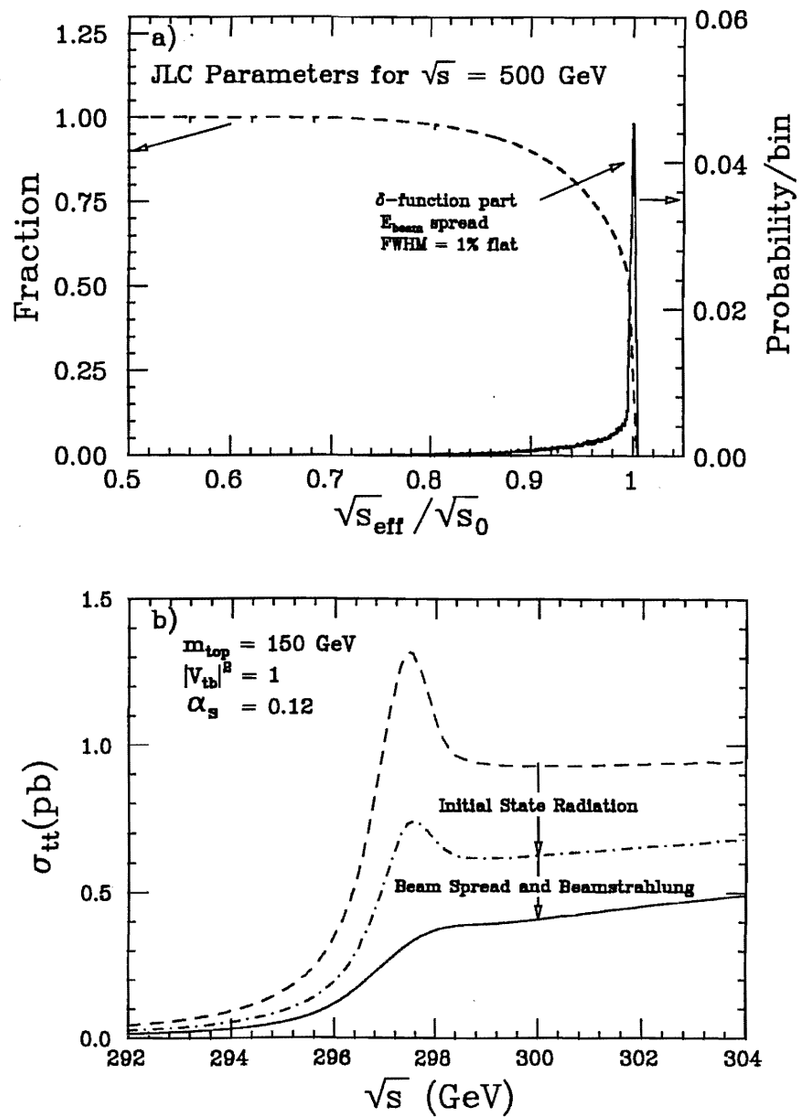
a)
JLC Parameters for √s = 500 GeV
δ−function part
E_beam spread
FWHM = 1% flat
Fraction
Probability/bin
√s_eff / √s_0
b)
m_top = 150 GeV
|V_tb|² = 1
α_s = 0.12
Initial State Radiation
Beam Spread and Beamstrahlung
σ_tt(pb)
√s (GeV)

Fig.7

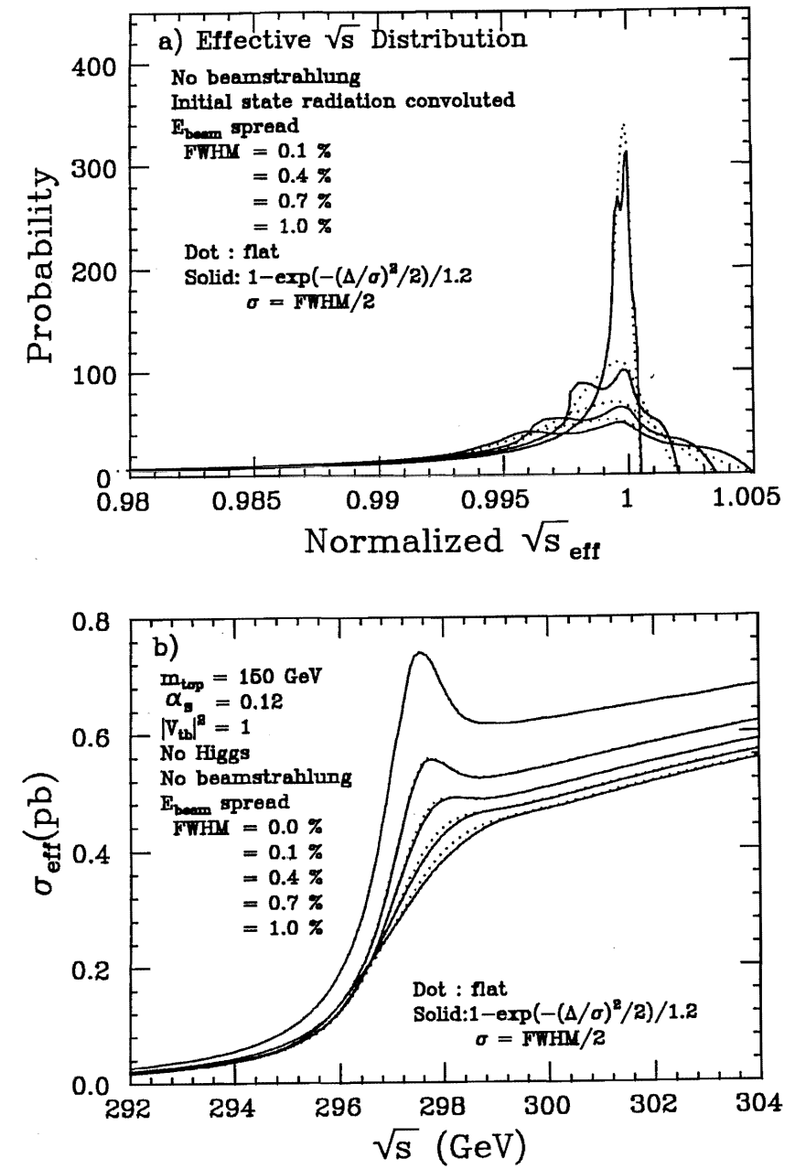
a) Effective √s Distribution
No beamstrahlung
Initial state radiation convoluted
E_beam spread
FWHM = 0.1 %
= 0.4 %
= 0.7 %
= 1.0 %
Dot : flat
Solid: 1−exp(−(Δ/σ)²/2)/1.2
σ = FWHM/2
Probability
Normalized √s_eff
b)
m_top = 150 GeV
α_s = 0.12
|V_tb|² = 1
No Higgs
No beamstrahlung
E_beam spread
FWHM = 0.0 %
= 0.1 %
= 0.4 %
= 0.7 %
= 1.0 %
Dot : flat
Solid:1−exp(−(Δ/σ)²/2)/1.2
σ = FWHM/2
σ_eff(pb)
√s (GeV)

Fig.8

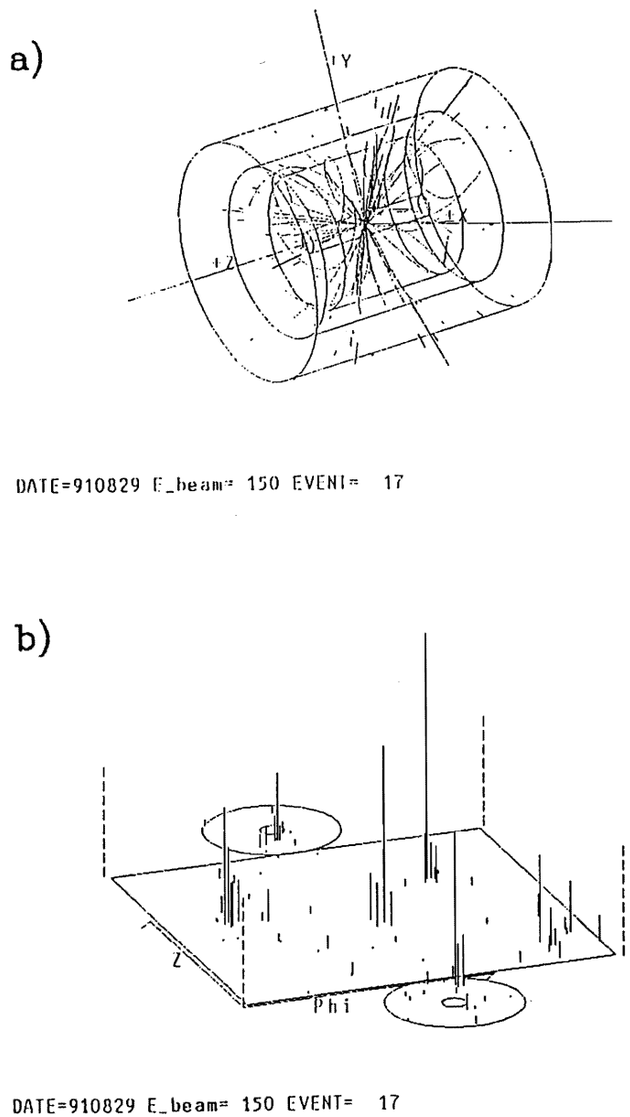
a)
+Y
+Z
DATE=910829 E_beam= 150 EVENT= 17
b)
Phi
Z
DATE=910829 E_beam= 150 EVENT= 17

Fig.9

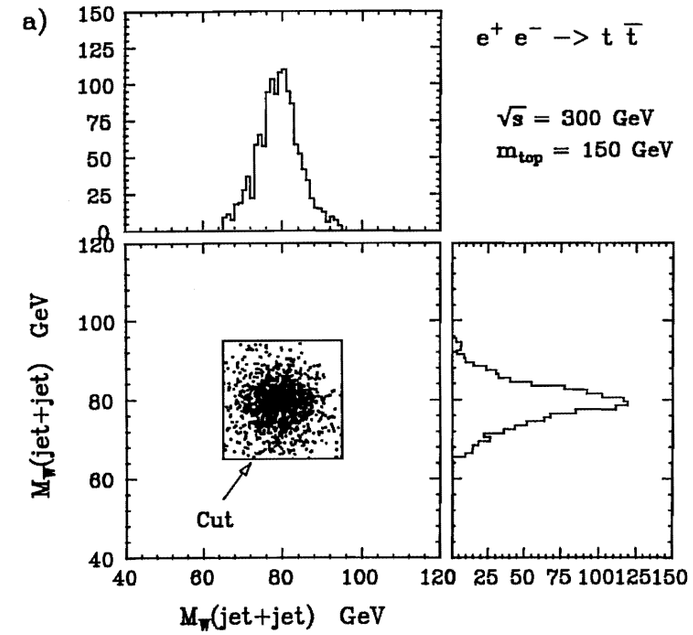
a)
$e^+ e^- \to t \bar{t}$
$\sqrt{s}$ = 300 GeV
m_{top} = 150 GeV
M_W(jet+jet) GeV
Cut
M_W(jet+jet) GeV

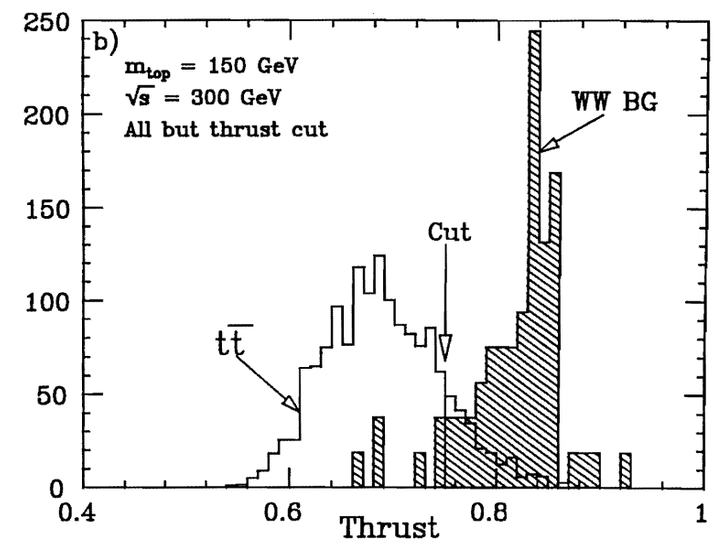
b)
m_{top} = 150 GeV
$\sqrt{s}$ = 300 GeV
All but thrust cut
WW BG
Cut
$t\bar{t}$
Thrust

Fig.10

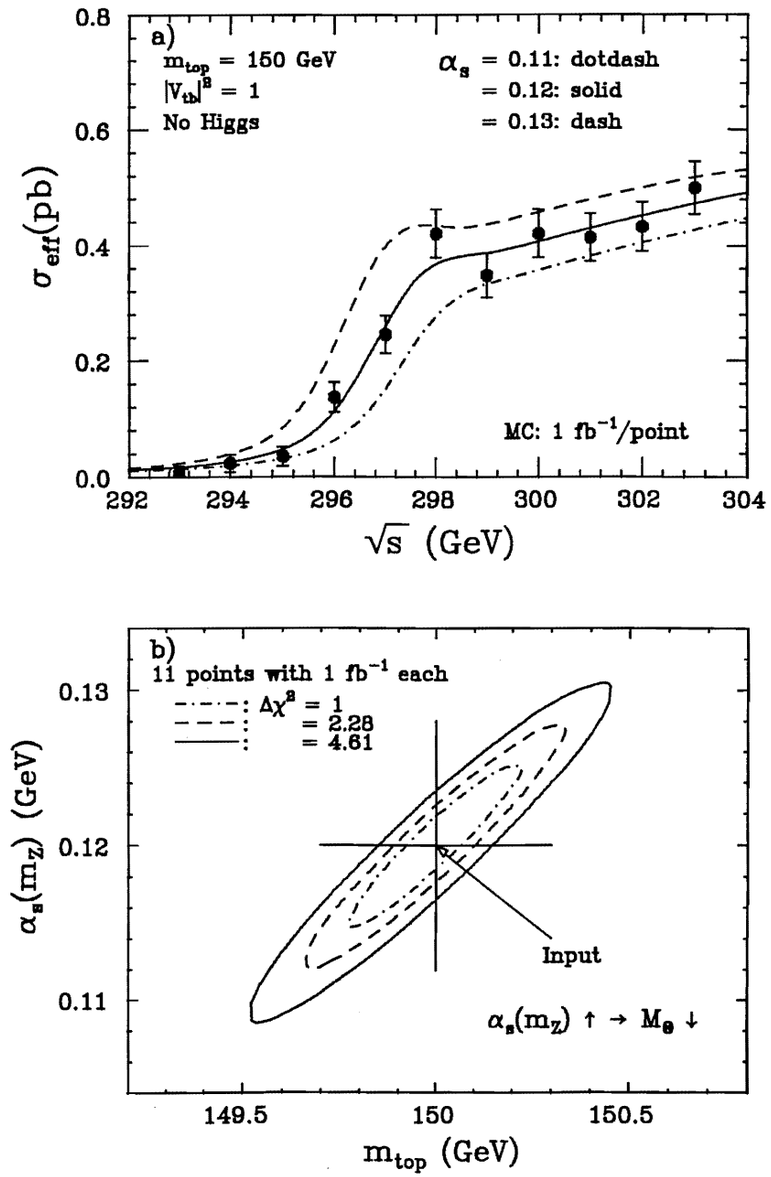
a)
m_{top} = 150 GeV
$|V_{tb}|^2$ = 1
No Higgs
α_s = 0.11: dotdash
= 0.12: solid
= 0.13: dash
MC: 1 fb^{-1}/point
σ_{eff}(pb)
$\sqrt{s}$ (GeV)
b)
11 points with 1 fb^{-1} each
$\Delta\chi^2$ = 1
= 2.28
= 4.61
Input
$\alpha_s(m_Z) \uparrow \rightarrow M_\Theta \downarrow$
$\alpha_s(m_Z)$ (GeV)
m_{top} (GeV)

Fig.11

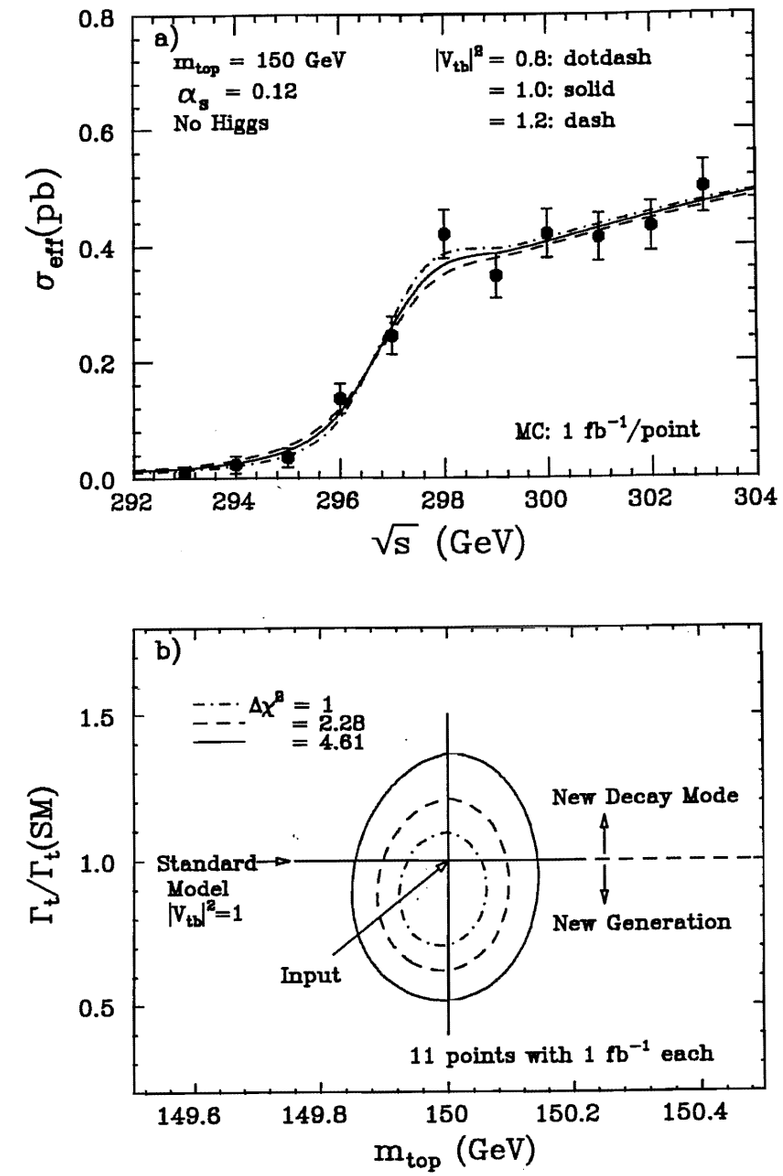
a)
m_{top} = 150 GeV
α_s = 0.12
No Higgs
$|V_{tb}|^2$ = 0.8: dotdash
= 1.0: solid
= 1.2: dash
MC: 1 fb^{-1}/point
σ_{eff}(pb)
$\sqrt{s}$ (GeV)
b)
$\Delta\chi^2$ = 1
= 2.28
= 4.61
New Decay Mode
Standard Model $|V_{tb}|^2$=1
New Generation
Input
11 points with 1 fb^{-1} each
Γ_t/Γ_t(SM)
m_{top} (GeV)

Fig.12

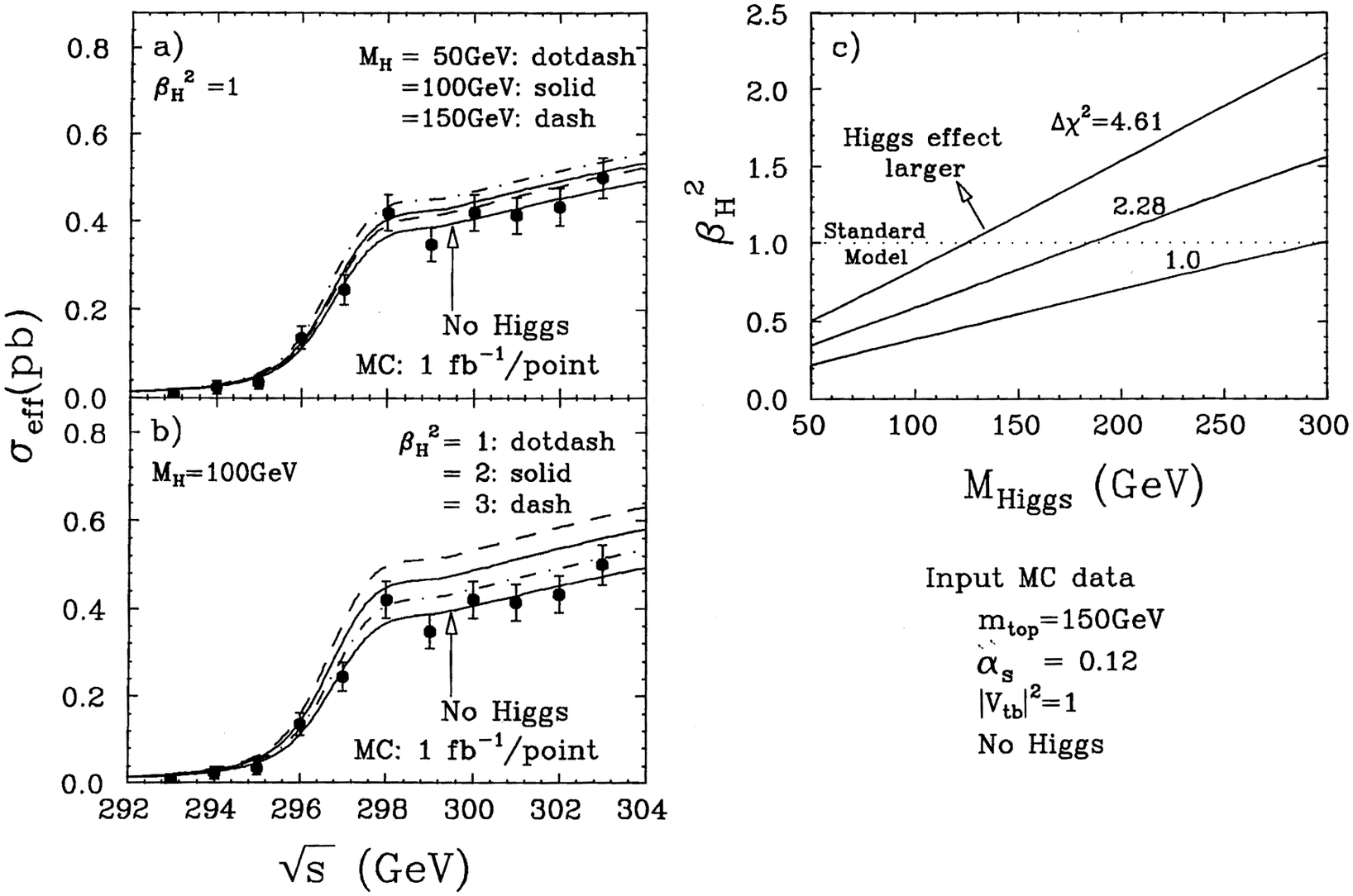
a)
β_H^2 =1
M_H = 50GeV: dotdash
=100GeV: solid
=150GeV: dash
No Higgs
MC: 1 fb^{-1}/point
b)
M_H=100GeV
β_H^2= 1: dotdash
= 2: solid
= 3: dash
No Higgs
MC: 1 fb^{-1}/point
σ_{eff}(pb)
$\sqrt{s}$ (GeV)
c)
Higgs effect
larger
$\Delta\chi^2$=4.61
2.28
1.0
Standard
Model
β_H^2
M_{Higgs} (GeV)
Input MC data
m_{top}=150GeV
α_s = 0.12
$|V_{tb}|^2$=1
No Higgs

Fig.13

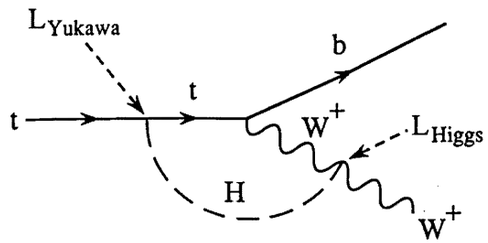

Fig.14

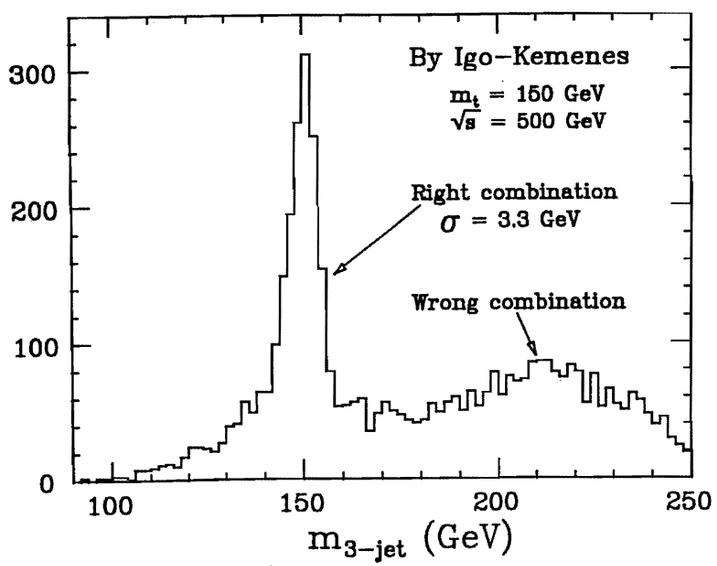

Fig.15

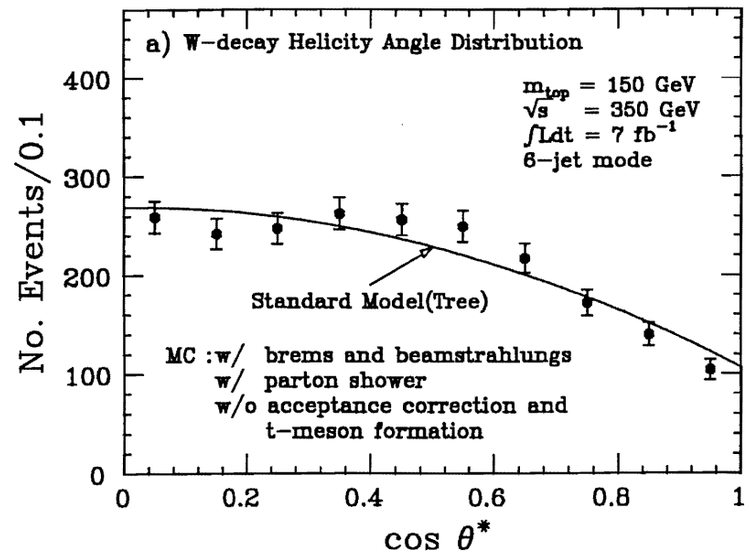

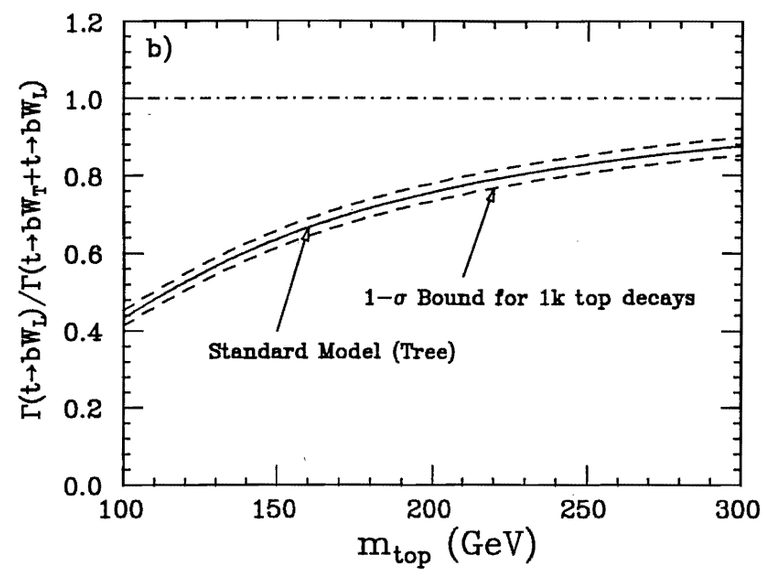

Fig.16

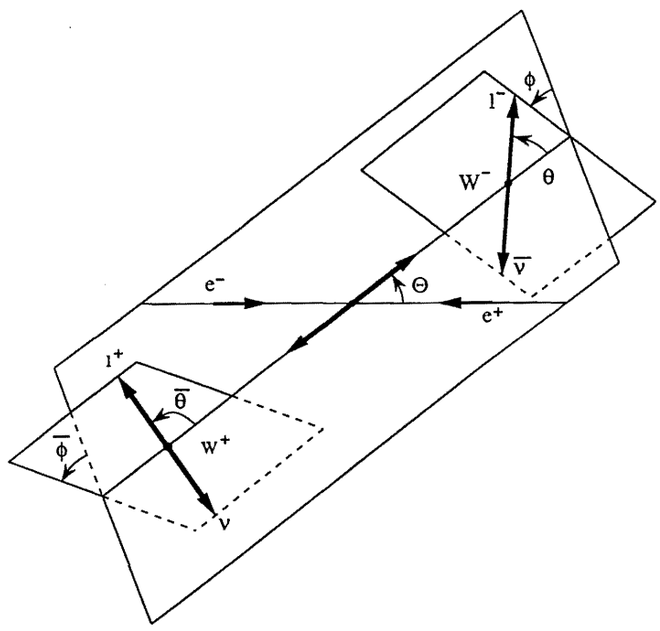
ϕ
l^-
W^-
θ
$\bar{\nu}$
e^-
Θ
e^+
l^+
$\bar{\theta}$
W^+
$\bar{\phi}$
ν

Fig.17

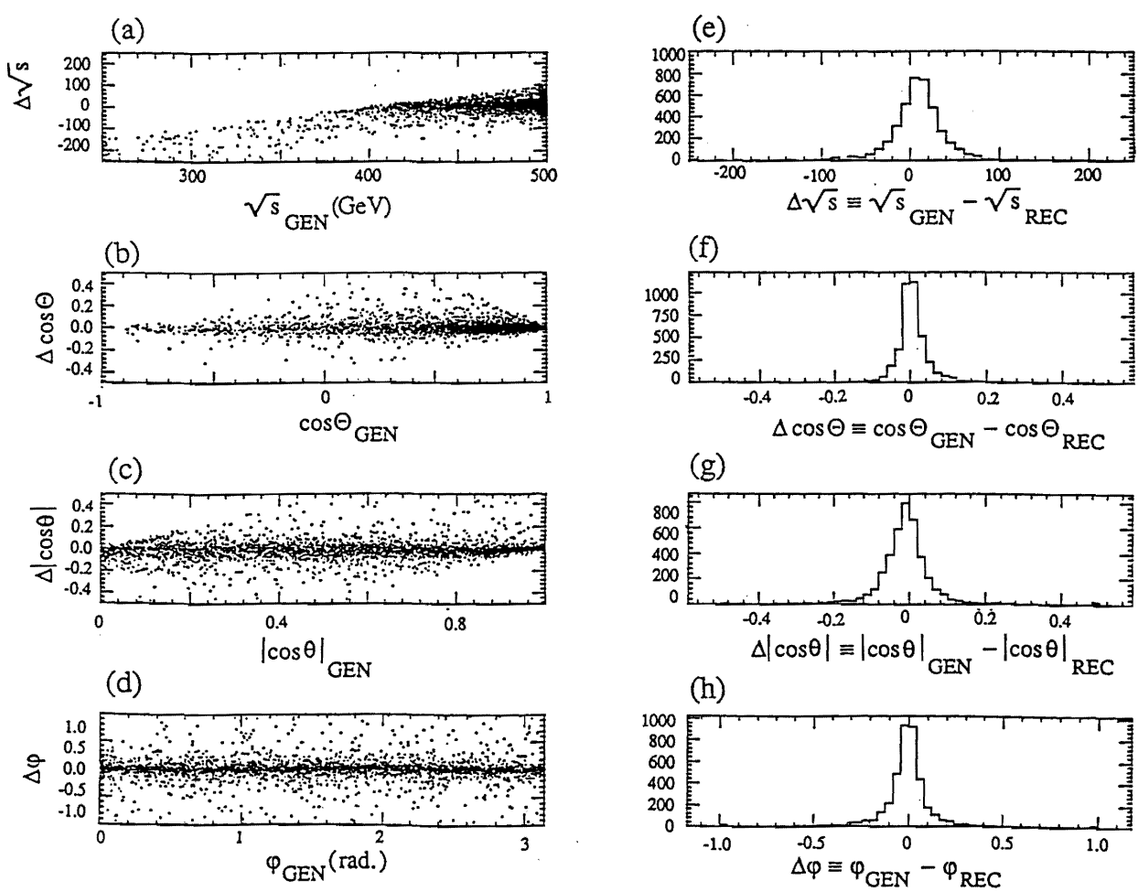
(a)
$\Delta\sqrt{s}$
$\sqrt{s}_{GEN}$(GeV)
(b)
$\Delta\cos\Theta$
$\cos\Theta_{GEN}$
(c)
$\Delta|\cos\theta|$
$|\cos\theta|_{GEN}$
(d)
$\Delta\varphi$
φ_{GEN}(rad.)
(e)
$\Delta\sqrt{s} \equiv \sqrt{s}_{GEN} - \sqrt{s}_{REC}$
(f)
$\Delta\cos\Theta \equiv \cos\Theta_{GEN} - \cos\Theta_{REC}$
(g)
$\Delta|\cos\theta| \equiv |\cos\theta|_{GEN} - |\cos\theta|_{REC}$
(h)
$\Delta\varphi \equiv \varphi_{GEN} - \varphi_{REC}$

Fig.18

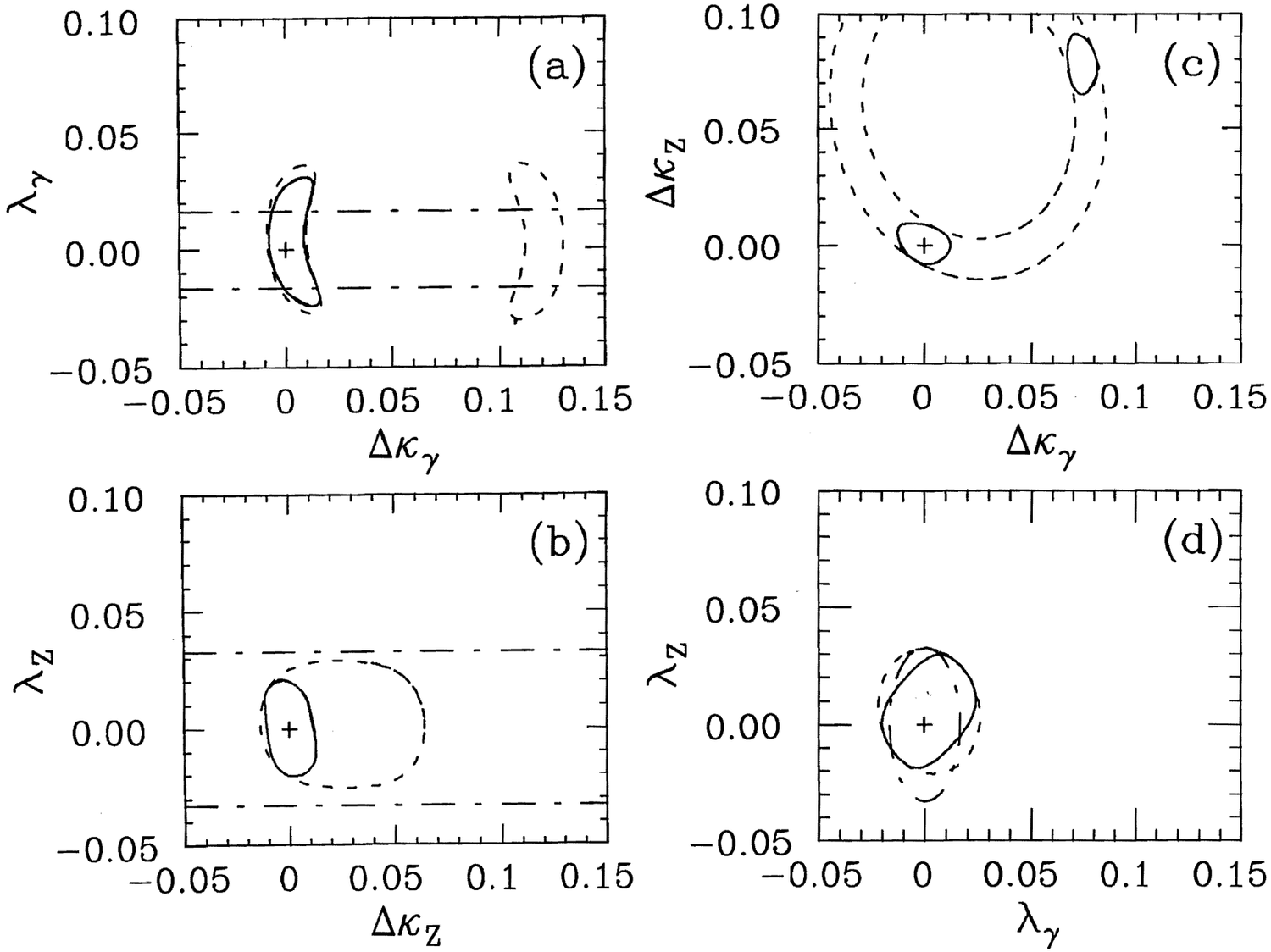
(a)
(b)
(c)
(d)
0.10
0.05
0.00
−0.05
−0.05
0
0.05
0.1
0.15
λ_γ
$\Delta\kappa_\gamma$
λ_Z
$\Delta\kappa_Z$

Fig.19

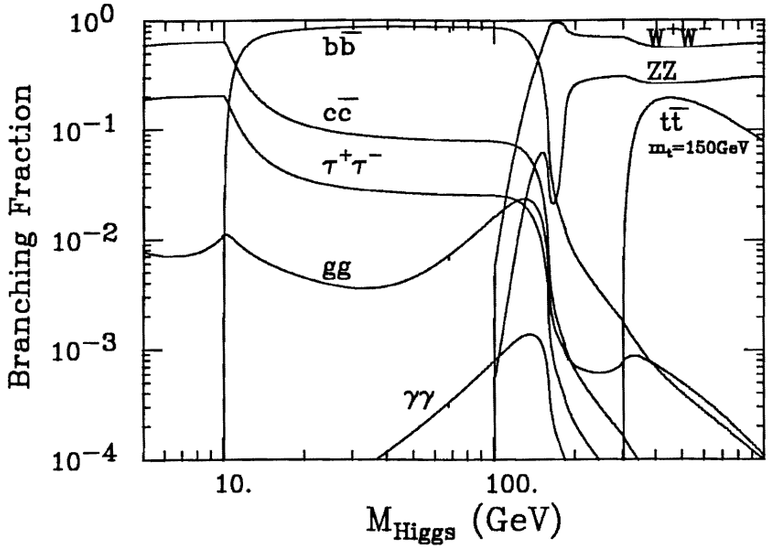

Fig.20

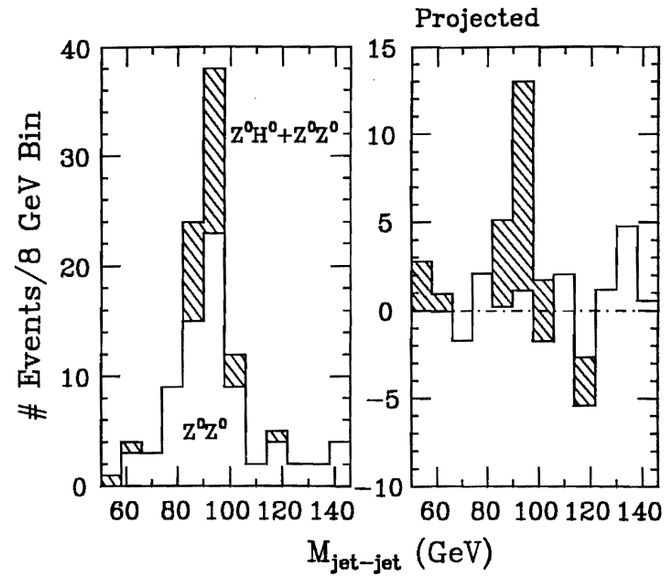

Fig.22

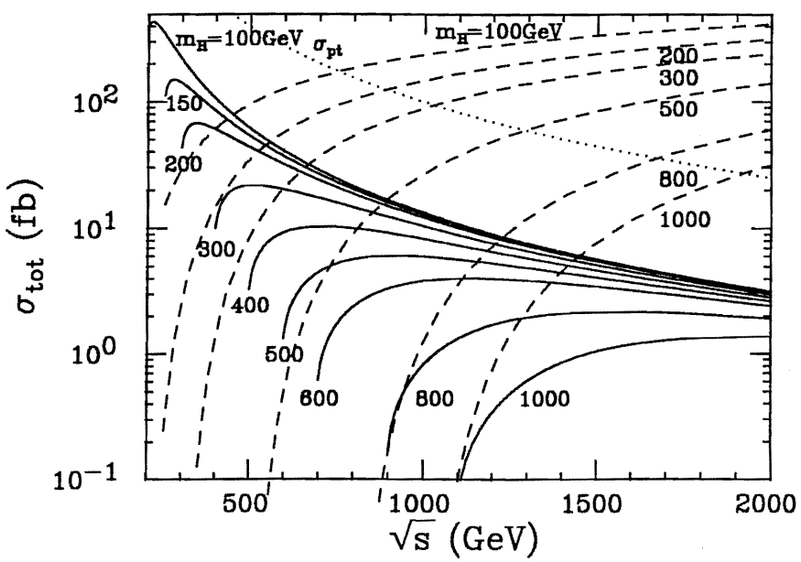

Fig.21

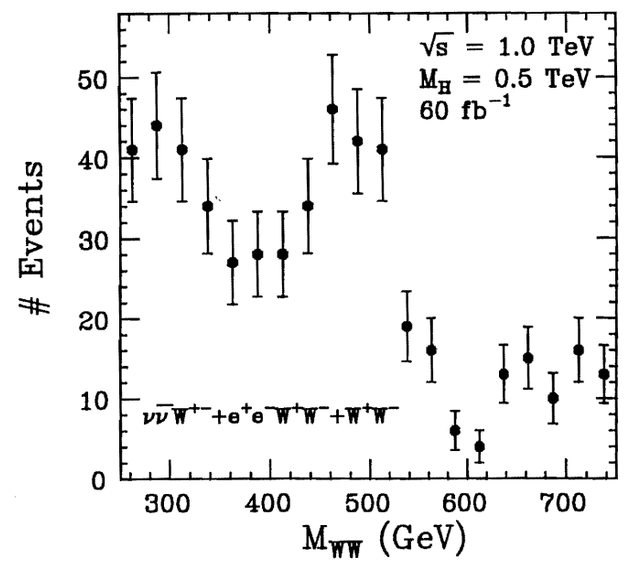

Fig.23

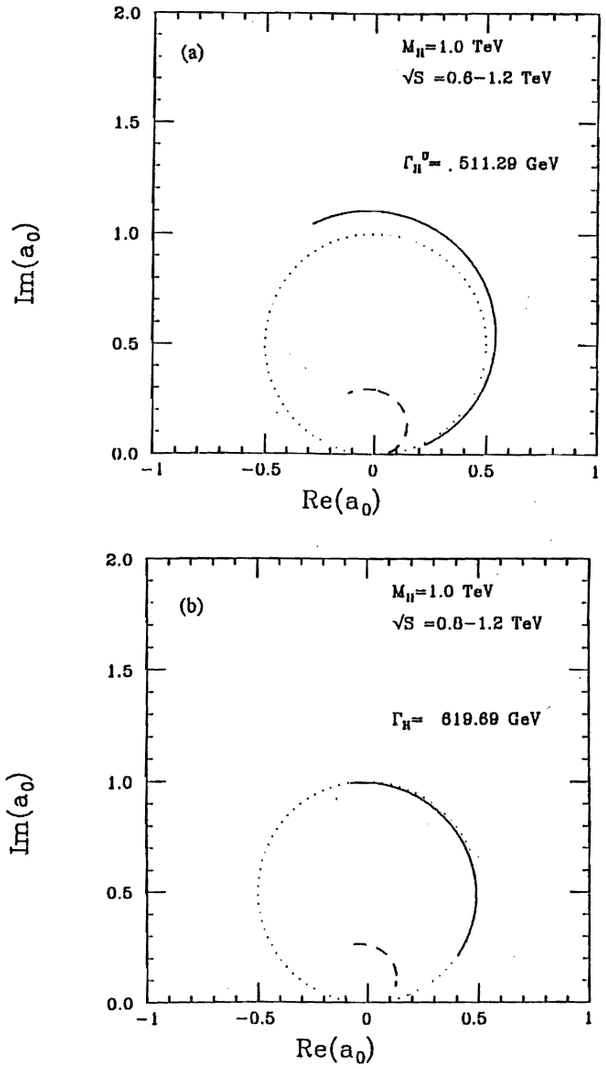

Fig.24

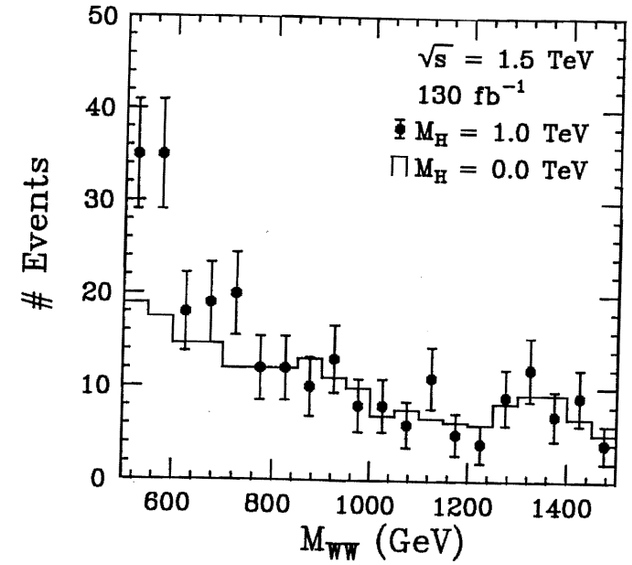

Fig.25

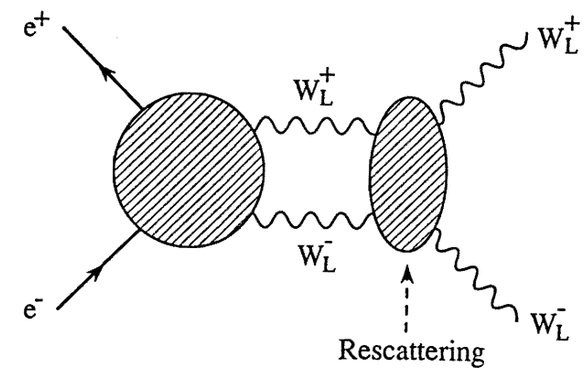

Fig.26

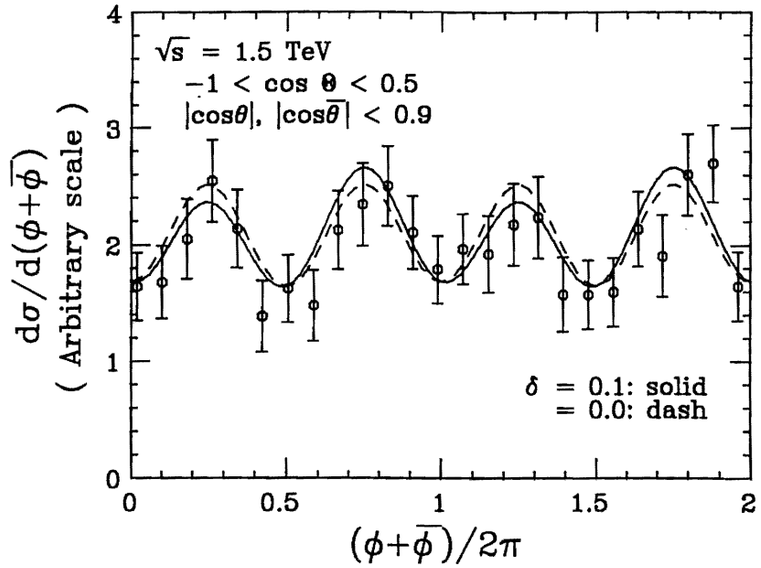

Fig.27

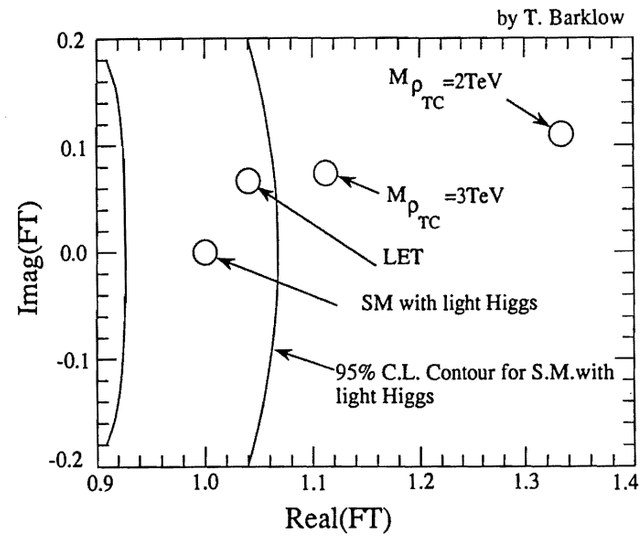

Fig.29

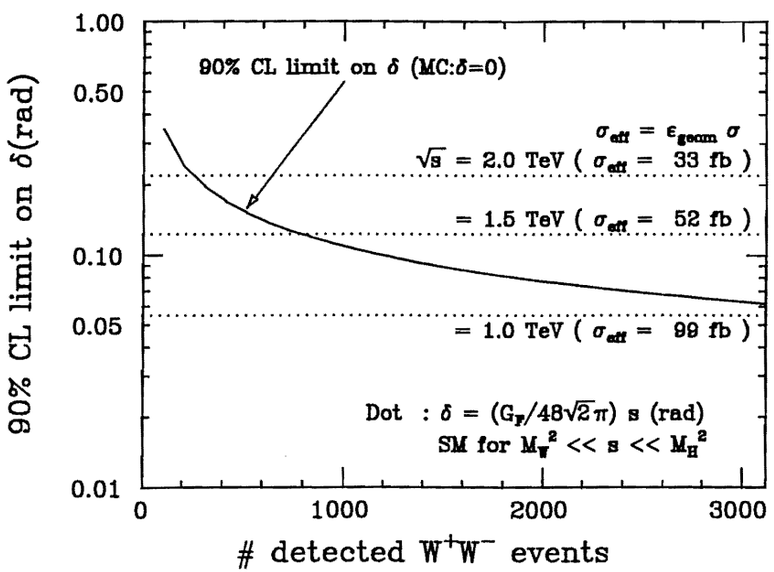

Fig.28

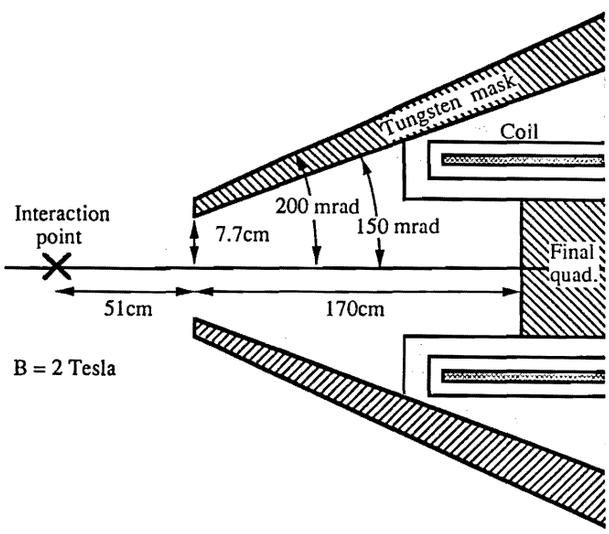

Fig.30

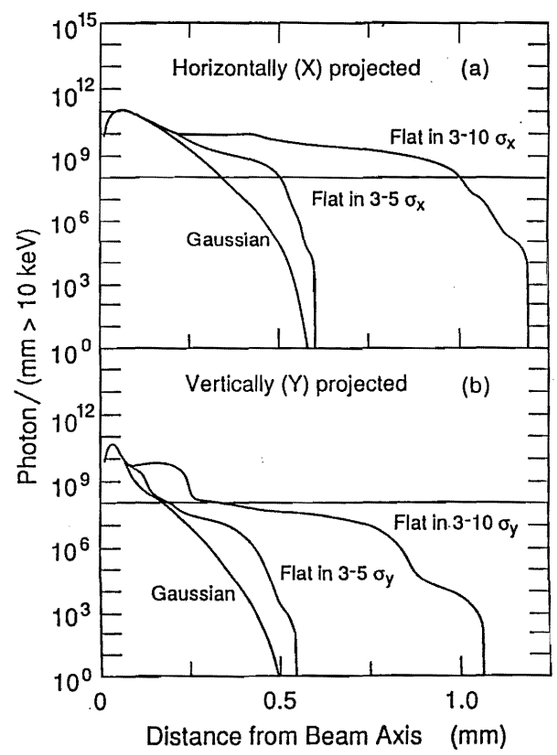

Fig.31

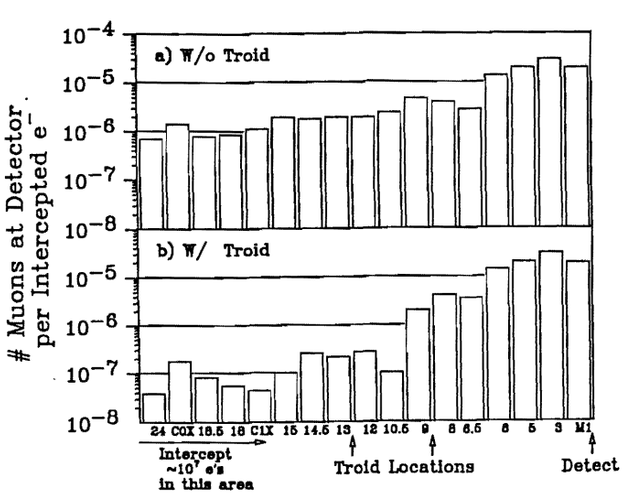

Fig.32

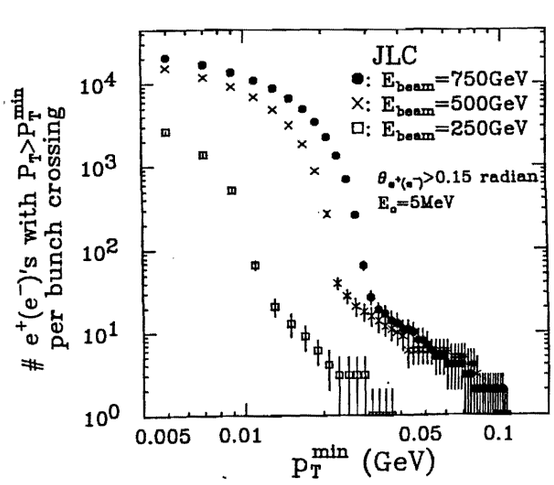

Fig.33

a) Direct

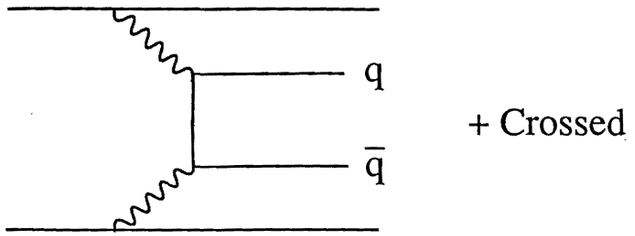

b) Once resolved

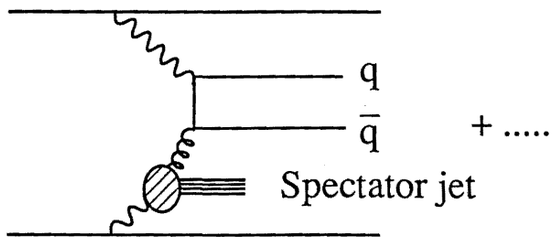

c) Twice resolved

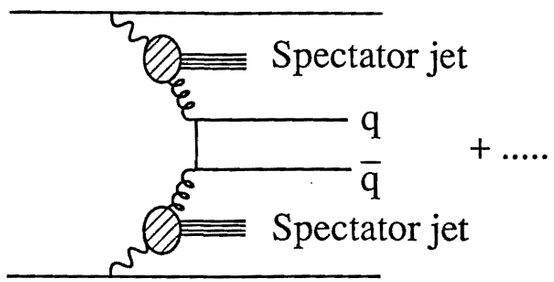

Fig.34

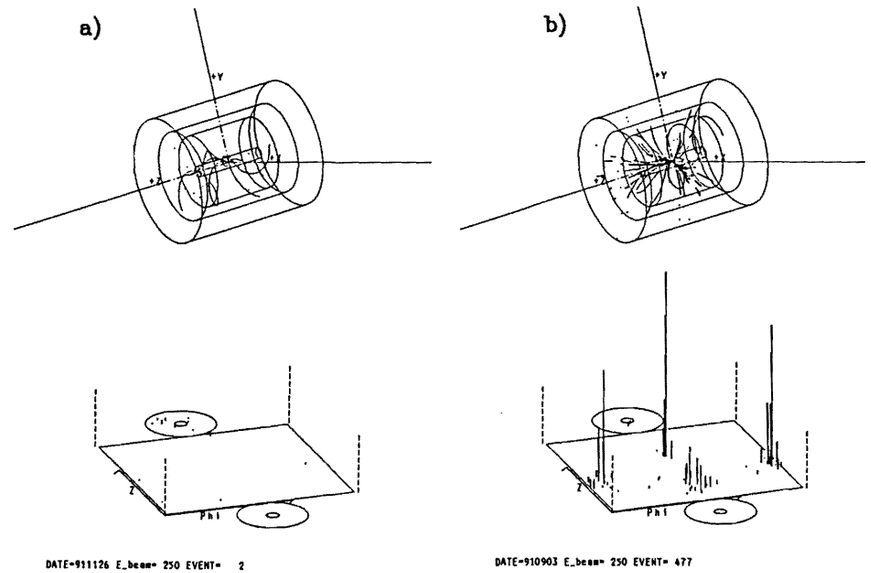

Fig.35

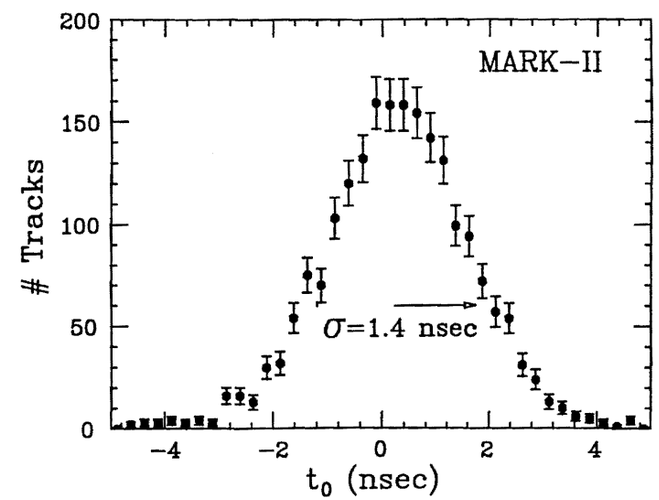

Fig.36